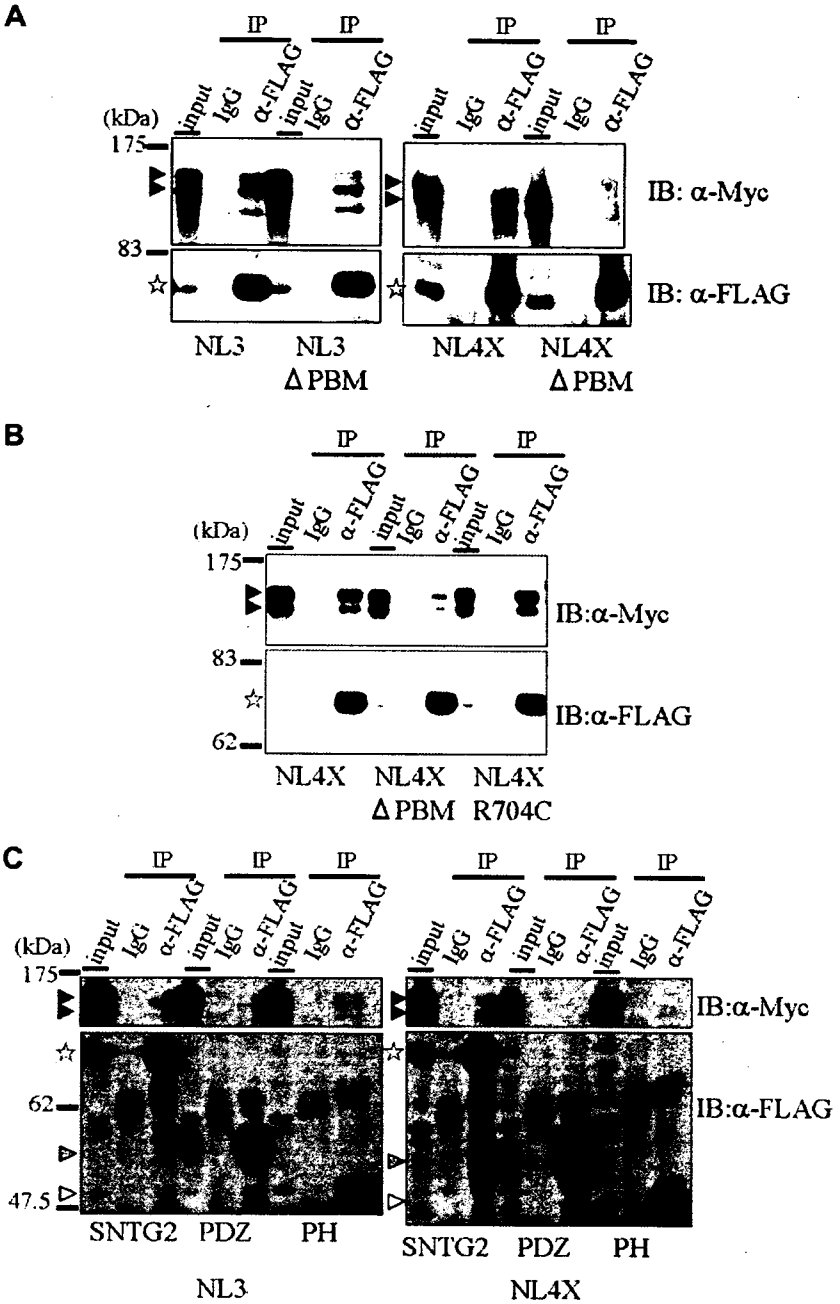

Fig. 3. (A) Effects of the deletion of PBM in NLs on the binding between SNTG2 and NLs in COS-7 cells. Various Myc-tagged NLs were co-immunoprecipitated with FLAG-SNTG2 in Lysis buffer. The deletion of PBM in NLs weakened the binding of NLs to SNTG2. Arrowheads and stars indicate Myc-NLs and FLAG-SNTG2, respectively. (B) The effect of R704C in NL4X, the autism-related mutation, on the binding to SNTG2 in COS-7 cells. Various Myc-tagged NL4Xs were co-immunoprecipitated with FLAG-SNTG2 in Lysis buffer. Under these conditions, the effect of the R704C mutation on the binding to SNTG2 was not detected. (C) The role of PDZ or the PH domain of SNTG2 in binding to NL. Whenever the regions containing the PDZ or PH domain were deleted, binding to NL was weakened. Therefore, both these regions might be involved in the interaction between NL and SNTG2. Black, gray, and white arrowheads and the star indicate Myc-NLs, the FLAG-tagged region containing the PDZ domain, the FLAG-tagged region containing the PH domain of SNT2G2, and the FLAG-tagged full-length SNTG, respectively.

in comparison with other parts of NL. These findings led us to hypothesize that due to the diversity of TMD32, NLs are functionally different from each other and the sequence of TMD32 for each NL determines whether the NL localizes in the inhibitory synapse. In this experiment, we could not examine the interaction between SNTG2 and NL2, which has been reported to localize in the inhibitory synapse exclusively. However, NL2 is

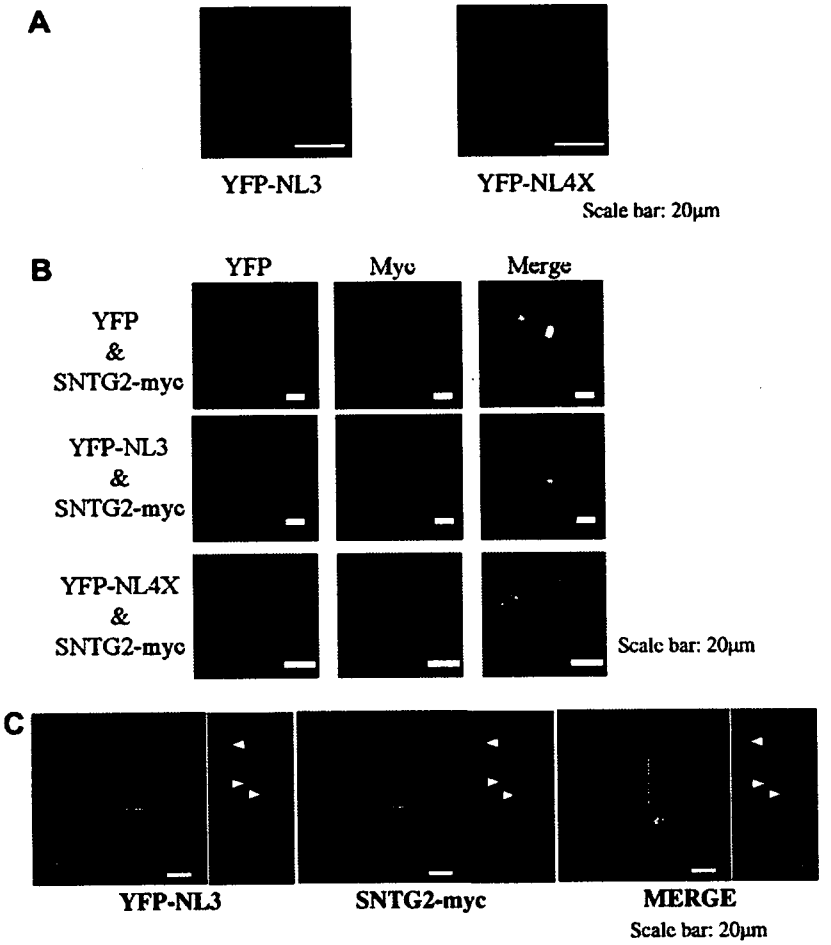

Fig. 4. (A) Localization of NL3 and NL4X on the surface of COS-7 cells. Only YFP-NL3 and YFP-NL4X on the cell-surface were immunostained using anti-GFP antibody and the secondary antibody conjugated with Oregon Green 488 without membrane permeabilization. They were clustered on the cell surface. (B) Localization of NLs and SNTG2 in COS-7 cells. The upper panels are negative controls. YFP or YFP-NL of cell-surface, SNTG2-Myc and merged images are shown on the left, center, and right, respectively. Co-transfected YFP-NL and SNTG2-Myc partially colocalized. Scale bar, 20 μm. (C) Localization of NL3, NL4X, and SNTG2 in rat cortical neurons. Neurons were transfected with YFP-NL3 and SNTG2-Myc at DIV7 using Lipofectamine 2000. After a 48-h incubation, the neurons were fixed, immunostained, and observed under confocal microscopy. The boxed area is enlarged in the bottom row. The clusters of YFP-NL3 of cell-surface sometimes colocalized with the cluster of SNTG2-Myc (arrowhead). Scale bar, 20 μm.

expected to bind to SNTG2 much stronger than any other NL, considering that both NL2 and SNTG2 dominantly localize in the inhibitory synapse [13,14,16]. The interaction will be determined in future.

Recently, some reports have suggested that the balance between excitatory and inhibitory synapses is disrupted in patients with autism [17,18]. A postmortem analysis of the brains of subjects with autism indicated that glutamic acid decarboxylase (GAD) was reduced in the autistic parietal and cerebellar cortices [11], suggesting that the impairment of GABAergic synaptic transmission causes autism. Meanwhile, the binding of NLs to SNTG2, a putative inhibitory-synaptic scaffolding protein, were affected by autism-related mutations in *NLs* in our experiments. Totally, the interactions between NLs and SNTG2 at the inhibitory synapse may be deeply involved in the etiology of autism. In future, screening autistic individuals for *SNTG2* mutations may elucidate the association between autism and the binding of SNTG2 to NLs.

References

[1] K. Ichtchenko, Y. Hata, T. Nguyen, B. Ullrich, M. Missler, C. Moomaw, T.C. Sudhof, Neuroligin 1: a splice site-specific ligand for beta-neurexins, Cell 81 (1995) 435–443.
[2] E.R. Graf, X. Zhang, S.X. Jin, M.W. Linhoff, A.M. Craig, Neurexins induce differentiation of GABA and glutamate postsynaptic specializations via neuroligins, Cell 119 (2004) 1013–1026.
[3] C. Dean, F.G. Scholl, J. Choih, S. DeMaria, J. Berger, E. Isacoff, P. Scheiffele, Neurexin mediates the assembly of presynaptic terminals, Nat. Neurosci. 6 (2003) 708–716.

[4] P. Scheiffele, J. Fan, J. Choih, R. Fetter, T. Serafini, Neuroligin expressed in nonneuronal cells triggers presynaptic development in contacting axons, Cell 101 (2000) 657–669.
[5] S. Jamain, H. Quach, C. Betancur, M. Rastam, C. Colineaux, I.C. Gillberg, H. Soderstrom, B. Giros, M. Leboyer, C. Gillberg, et al., Mutations of the X-linked genes encoding neuroligins NLGN3 and NLGN4 are associated with autism, Nat. Genet. 34 (2003) 27–29.
[6] B. Chih, S.K. Afridi, L. Clark, P. Scheiffele, Disorder-associated mutations lead to functional inactivation of neuroligins, Hum. Mol. Genet. 13 (2004) 1471–1477.
[7] D. Comoletti, A. De Jaco, L.L. Jennings, R.E. Flynn, G. Gaietta, I. Tsigelny, M.H. Ellisman, P. Taylor, The Arg451Cys-neuroligin-3 mutation associated with autism reveals a defect in protein processing, J. Neurosci. 24 (2004) 4889–4893.
[8] F. Laumonnier, F. Bonnet-Brilhault, M. Gomot, R. Blanc, A. David, M.P. Moizard, M. Raynaud, N. Ronce, E. Lemonnier, P. Calvas, et al., X-linked mental retardation and autism are associated with a mutation in the NLGN4 gene, a member of the neuroligin family, Am. J. Hum. Genet. 74 (2004) 552–557.
[9] J. Yan, G. Oliveira, A. Coutinho, C. Yang, J. Feng, C. Katz, J. Sram, A. Bockholt, I.R. Jones, N. Craddock, et al., Analysis of the neuroligin 3 and 4 genes in autism and other neuropsychiatric patients, Mol. Psychiatry 10 (2005) 329–332.
[10] M.M. Menold, Y. Shao, C.M. Wolpert, S.L. Donnelly, K.L. Raiford, E.R. Martin, S.A. Ravan, R.K. Abramson, H.H. Wright, G.R. Delong, et al., Association analysis of chromosome 15 gabaa receptor subunit genes in autistic disorder, J. Neurogenet. 15 (2001) 245–259.
[11] S.H. Fatemi, A.R. Halt, J.M. Stary, R. Kanodia, S.C. Schulz, G.R. Realmuto, Glutamic acid decarboxylase 65 and 67 kDa proteins are reduced in autistic parietal and cerebellar cortices, Biol. Psychiatry 52 (2002) 805–810.
[12] M.E. Adams, N. Kramarcy, T. Fukuda, A.G. Engel, R. Sealock, S.C. Froehner, Structural abnormalities at neuromuscular synapses lacking multiple syntrophin isoforms, J. Neurosci. 24 (2004) 10302–10309.
[13] G. Piluso, M. Mirabella, E. Ricci, A. Belsito, C. Abbondanza, S. Servidei, A.A. Puca, P. Tonali, G.A. Puca, V. Nigro, Gamma1- and gamma2-syntrophins, two novel dystrophin-binding proteins localized in neuronal cells, J. Biol. Chem. 275 (2000) 15851–15860.
[14] I. Brunig, A. Suter, I. Knuesel, B. Luscher, J.M. Fritschy, GABAergic terminals are required for postsynaptic clustering of dystrophin but not of GABA(A) receptors and gephyrin, J. Neurosci. 22 (2002) 4805–4813.
[15] T. Dresbach, A. Neeb, G. Meyer, E.D. Gundelfinger, N. Brose, Synaptic targeting of neuroligin is independent of neurexin and SAP90/PSD95 binding, Mol. Cell Neurosci. 27 (2004) 227–235.
[16] F. Varoqueaux, S. Jamain, N. Brose, Neuroligin 2 is exclusively localized to inhibitory synapses, Eur. J. Cell Biol. 83 (2004) 449–456.
[17] H. Cline, Synaptogenesis: a balancing act between excitation and inhibition, Curr. Biol. 15 (2005) R203–R205.
[18] N.K. Hussain, M. Sheng, Neuroscience. Making synapses: a balancing act, Science 307 (2005) 1207–1208.

American Journal of Medical Genetics Part A 143A:2804–2809 (2007)

Clinical Report

22q13 Microduplication in Two Patients With Common Clinical Manifestations: A Recognizable Syndrome?

Nobuhiko Okamoto,[1]* Takeo Kubota,[2] Yutaka Nakamura,[3] Ryusuke Murakami,[3] Toshiya Nishikubo,[4] Ichiro Tanaka,[4] Yukihiro Takahashi,[4] Shin Hayashi,[5] Issei Imoto,[5] Johji Inazawa,[5] Noboru Hosokai,[6] Shinichi Kohsaka,[7] and Shigeo Uchino[7]

[1]Department of Planning and Research, Osaka Medical Center and Research Institute for Maternal and Child Health, Osaka, Japan

[2]Department of Epigenetic Medicine, Interdisciplinary Graduate School of Medicine and Engineering, University of Yamanashi, Yamanashi, Japan

[3]Department of Pediatrics, Awaji Prefecutural Hopsital, Hyogo, Japan

[4]Department of Pediatrics, Nara Medical University, Nara, Japan

[5]Department of Molecular Cytogenetics, Medical Research Institute, Tokyo Medical and Dental University, Tokyo, Japan

[6]Research and Development Division, Mitsubishi Kagaku Bio-Clinical Laboratory, Tokyo, Japan

[7]Department of Neurochemistry, National Institute of Neuroscience, Kodaira, Tokyo, Japan

Received 15 September 2007; Accepted 10 February 2007

We report here on two unrelated patients (Patients 1 and 2) with a cryptic microduplication involving a 22q13 segment. Both patients manifested infantile hypotonia, developmental delay, and growth deficiency. In addition, an abnormal signal intensity area was detected in the frontal white matter of Patient 2 by brain MRI. Whole-genome microarray comparative genomic hybridization for Patient 1 and fluorescence in situ hybridization analysis with 22q-subtelomeric probes performed in both patients showed a submicroscopic 22q13 duplication that involved the *SHANK3* gene. The duplication in Patient 1 was de novo type, while that in Patient 2 was derived from a familial 17;22 translocation. The presence of common clinical manifestations in the two patients with the common duplicated region led to a conclusion that 22q terminal duplication is a recognizable clinical entity, that is, the 22q13 microduplication syndrome. © 2007 Wiley-Liss, Inc.

Key words: comparative genomic hybridization; the 22q13 microduplication syndrome; the 22q13 deletion syndrome; mental retardation; *SHANK3*

How to cite this article: Okamoto N, Kubota T, Nakamura Y, Murakami R, Nishikubo T, Tanaka I, Takahashi Y, Hayashi S, Imoto I, Inazawa J, Hosokai N, Kohsaka S, Uchino S. 2007. 22q13 microduplication in two patients with common clinical manifestations: A recognizable syndrome? Am J Med Genet Part A 143A:2804–2809.

INTRODUCTION

Terminal 22q13 deletion (the Phelan-McDermid syndrome, PMS) is one of diseases with submicroscopic telomere deletions [Phelan et al., 2001]. PMS is characterized by significant expressive language delay, mental retardation, hypotonia, minor craniofacial dysmorphisms (dolichocephaly, epicanthal folds, saddle nose with bulbous tip, abnormal ears, ptosis of eyelids), dysplastic toenails, increased tolerance to pain, relatively large hands and normal to advanced growth. Autistic features are often observed [Manning et al., 2004]. As there was a correlation between clinical features and deletion size, haploinsufficiency of the *SHANK3* (or *ProSAP2*) gene expressed in the cerebral cortex and cerebellum is thought as a major factor in the neurological symptoms of PMS [Bonaglia et al., 2001; Wilson et al., 2003; Koolen et al., 2005]. Recently, mutations in the

Grant sponsor: Ministry of Education, Culture, Sports, Science and Technology; Grant sponsor: Osaka Medical Center and Research Institute; Grant sponsor: Ministry of Health, Labor and Welfare of Japan.

*Correspondence to: Dr. Nobuhiko Okamoto, Department of Planning and Research, Osaka Medical Center and Research Institute for Maternal and Child Health, 840 Murodo-cho, Izumi, Osaka 594-1101, Japan.
E-mail: okamoto@osaka.email.ne.jp

DOI 10.1002/ajmg.a.31771

SHANK3 gene were found in the patients with autism spectrum disorders [Durand et al., 2007]. On the other hand, a duplication of a distal part of 22q is less frequent. Barajas-Barajas et al. [2004] summarized clinical findings of distal trisomy 22, that is, severe mental and growth retardation, failure to thrive, congenital hypotonia, hydrocephalus, microcephaly, epicanthic folds, low-set ears, broad prominent nasal bridge, cleft palate, long philtrum, micrognathia, finger-like thumbs and cryptorchidism. Feenstra et al. [2006] reported three patients with cryptic duplication of a distal segment of 22q.

We encountered two unrelated patients with a submicroscopic duplication of 22q13. Here we describe their clinical manifestations and propose their disorder as a recognizable syndrome.

MATERIALS AND METHODS

Patient 1

The patient, a 4-year-old girl, was the first child of nonconsanguineous healthy parents. Family history was unremarkable. She was born at 37 weeks gestation weighing 2,600 g (mean), 46 cm in length (−0.5 SD) and OFC of 32 cm (+1 SD). At age 4 months, she was referred to us because of generalized hypotonia and developmental delay. She started to walk unaided at 3½ years. Her mental development was moderately delayed. She used several meaningful words and could understand simple sentences. Her development quotient (DQ) was 40 estimated by the standard method. Craniofacial abnormalities noted included round face, prominent forehead, hypertelorism, arched eyebrows, downslanting palpebral fissures, broad and flat nasal bridge, shallow philtrum, low-set deformed ears and high-arched palate (Fig. 1a). She also had mild hypopigmentation of the skin and hair. Routine laboratory investigations were normal. Her G-banded karyotype was 46,XX. Her height, weight and OFC at age 4 years were 87 cm (−3.2 SD), 11.6 kg (−2.1 SD), and 46.0 cm (−2.6 SD), respectively. Brain MRI showed no significant abnormalities. EEG revealed sporadic spikes in the bilateral frontal areas. No epileptic seizures have been observed.

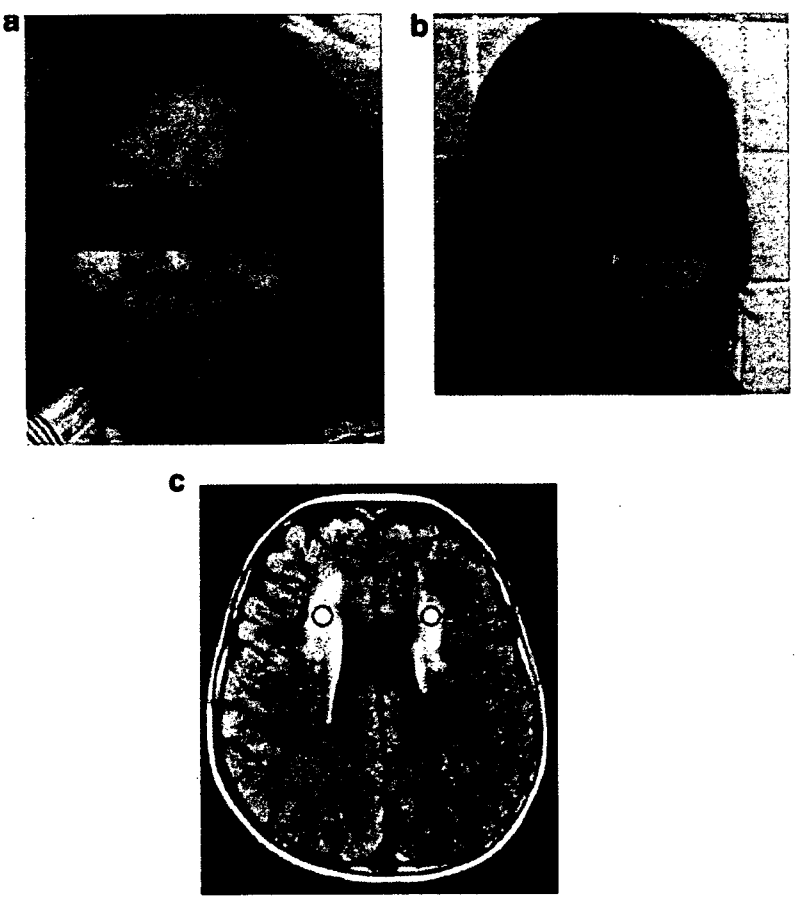

FIG. 1. Frontal view of Patient 1 at age 4 years (**a**) and Patient 2 at 6 years (**b**), and brain MRI (FLAIRE image) of Patient 2 showing prominent white matter lesions (indicated by circles) (**c**). [Color figure can be viewed in the online issue, which is available at www.interscience.wiley.com.]

Her character was affective and friendly, but not autistic.

Patient 2

The patient, a 6-year-old girl, was the second child of nonconsanguineous healthy parents. Her brother had severe developmental delays with a characteristic facial appearance. She was born at 40 weeks gestation. Her birth weight was 2,640 g (−0.9 SD), body length 45 cm (−1.6 SD), and OFC 32.8 cm (−0.4 SD). She was referred to us because of feeding difficulty. She was noted to have the following craniofacial abnormalities: round face, prominent forehead, hypertelorism, epicanthal folds, arch-shaped eyebrows, downslanting palpebral fissures, broad and flat nasal bridge, low-set deformed ears and high-arched palate (Fig. 1b). Her developmental milestones were delayed with estimated DQ of 46. She started to walk unaided at age $2^{4}/_{12}$ years. At age 6 years, she could understand simple sentences and speak several meaningful words. Initial standard G-banded karyotyping did not detect any abnormality and revealed 46,XX. Her height at age 6 years was 99.5 cm (−3.1 SD). Brain MRI showed abnormal signal intensity in the frontal white matter. The lesion was hypointense in T1-weighted image and hyperintense in T2-weighted image, whereas fluid-attenuated inversion recovery (FLAIR) image clearly demonstrated the white matter lesions (Fig. 1c). Screening for metabolic disorders was normal. Partial GH deficiency was found, and a replace therapy was started.

Analysis With Microarray Comparative Genomic Hybridization (CGH) and Fluorescence In Situ Hybridization (FISH)

The studies were approved by the Ethics Committee in Osaka Medical Center and Research Institute for Maternal and Child Health.

Patient 1 was studied with CGH on high-density Whole-Genome Microarray containing 4,523 BAC/PAC clones covering the entire genome at intervals of approximately 0.7 Mb [Inazawa et al., 2004]. Detailed methods have been reported previously [Hayashi et al., 2005]. If copy-number changes are suspected, subsequent FISH analyses were performed using BAC clones within the region of interest as probes to confirm the changes on normal metaphase chromosomes. Consequently, a duplication of the genomic region at 22q13.31−q33 was found, and its size was approximately 6.0 Mb (Fig. 2). FISH analysis using the *SHANK3* probe revealed that the duplicated segment included *SHANK3* (Fig. 3a). The *ARSA* locus at 22q13 was also duplicated with a control probe for the 22q11.2 deletion syndrome (data not shown). FISH analyses of her parent's chromosomes were normal (data not shown). However, we could not

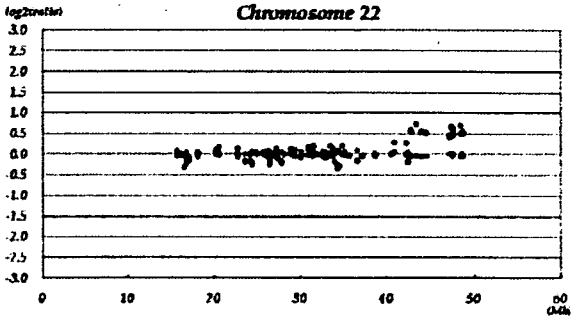

Fig. 2. Result of array CGH analysis of Patient 1. Each of the dots represents the $\log_2$ ratio of each BAC. Blue dots (arrow) represent results of the patient, whereas red dots represent average ratios from six independent healthy males. Copy number change in chromosome 22q13.31−13.33 is demonstrated. The duplication size was approximately 6.0 Mb. [Color figure can be viewed in the online issue, which is available at www.interscience.wiley.com.]

figure out orientation of the duplication because of its small size. Two color FISH with red and green signals showed one yellow signal. Because two patients with a distal 22q duplication derived from inv(22)(p13q12) in a parent have been reported by Barajas-Barajas et al. [2004], most plausible karyotype of Patient 1 was 46,XX.ish dup(22)(qter → q13::p13 → qter)dn.

Patient 2 and her brother were screened with FISH for subtelomeric abnormality using a fosmid clone containing important domains of *SHANK3* as a probe (BACPAC resources Center, Oakland, CA; Fig. 3b). By the analysis, her karyotype was correctly interpreted as 46,XX,der(17)t(17;22)(p13;q13). She inherited the derivative chromosome 17 from her father, who carries an apparently balanced cryptic reciprocal translocation involving the terminal regions of 17p and 22q. Duplicated segment including *SHANK3* was found at the short arm of chromosome 17 (Fig. 3b). The size of the 22q duplication was <2 Mb with further FISH analyses (Table I), and the deletion extent on chromosome 17 was <2.5 Mb from subtelomere, as the *LIS1* region was intact (data not shown). Her brother had a 46,XY,der(22)t(17;22)(p13;q13)pat karyotype.

DISCUSSION

Cryptic trisomy for distal 22q that contains the *SHANK3* gene was found in the present two patients. The trisomy in Patient 1 was de novo and that in Patient 2 was derived from paternal translocation, t(17;22)(p13;q13). The clinical manifestations of her brother whose karyotype was 46,XY,der(22)t(17;22)(p13;q13) were compatible with the 22q13 deletion syndrome (PMS). Both Patients 1 and 2 had infantile hypotonia, moderate developmental delay, and growth deficiency without visceral anomalies. Craniofacial features common to them were round face, prominent forehead, hypertelorism, arch-shaped eyebrows, downslanting palpebral

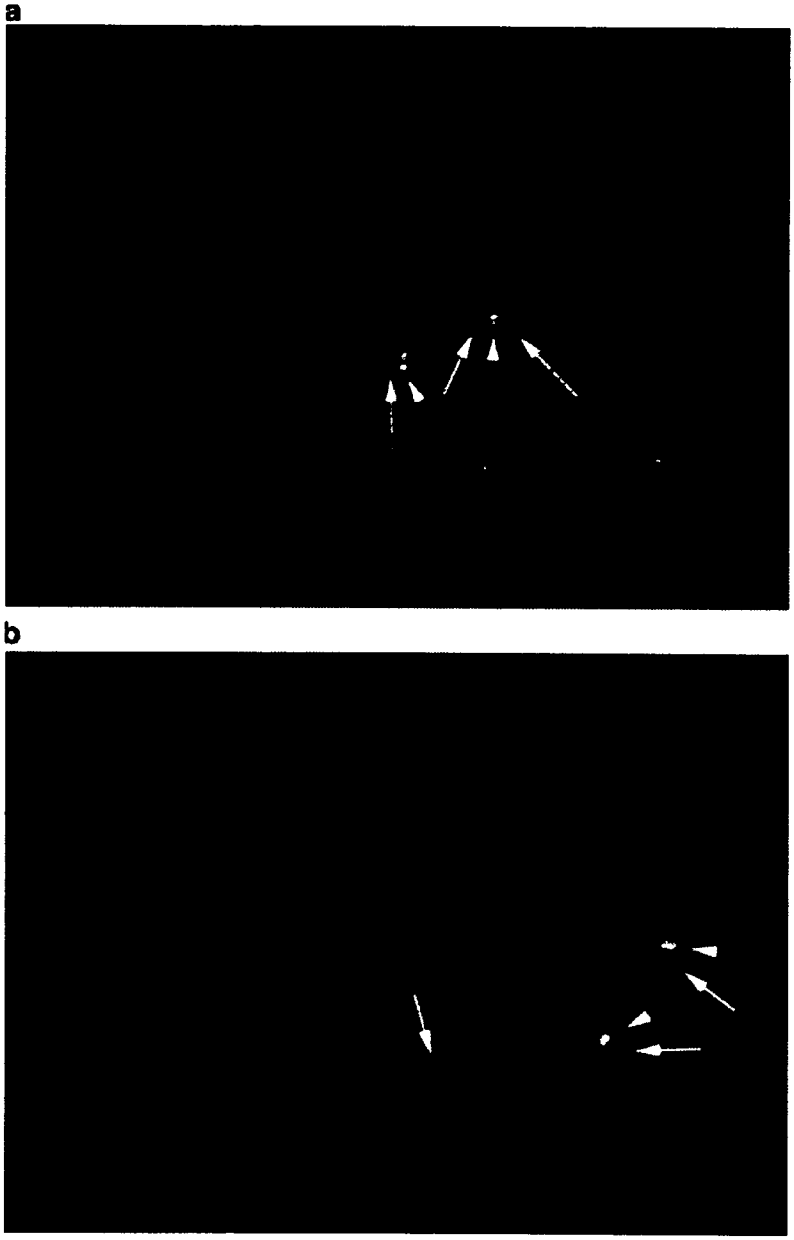

FIG. 3. FISH analysis of Patient 1 using a *SHANK3* probe (arrows) and 22q11 control probes (arrowheads) (**a**) showing a duplication of *SHANK3*. FISH of Patient 2 with the same probe showing another *SHANK3* signal on 17p in addition to two signals on chromosomes 22 (**b**). [Color figure can be viewed in the online issue, which is available at www.interscience.wiley.com.]

fissures, broad and flat nasal bridge, shallow philtrum and high-arched palate. The 22q-duplicated region in our two patients seems similar to the deleted region in PMS, in which the deletion extent varied from 130 kb to 9 Mb encompassing *SHANK3*. This is not surprising, especially in Patient 2, because her duplication was derived from familial t(17;22)(p13;q13) and reflect PMS in her brother as mentioned above.

There have been three reported cases of cryptic, terminal 22q duplication [Feenstra et al., 2006]. One of them carrying a terminal 22q duplication due to a de novo unbalanced translocation, der(21)t(21;22)(p13;q13.2) had some similarities in craniofacial features to both of our patients. Growth failure and moderate developmental delay were also common. On the other hand, although one of the patients reported by Feenstra et al. [2006] also

TABLE I. Probes Used for FISH Study of Patient 2

Chromosome band	Probe	Physical distance from telomere	Result of FISH
22cen			
22q 11.2	*TUPLE1*		N
22q 13.2	*RP11-794G14*	8 Mb	N
22q 13.31	*RP11-766K21*	6 Mb	N
22q 13.32	*RP11-53E22*	2 Mb	N
22q 13.33	*SHANK3*	0.1 Mb	D
	ARSA	3 kb	D
22qter			D

N, normal; D, duplication.

manifested pulmonary valve stenosis and ectopic kidney, neither of our patients had such visceral anomalies. The other two patients reported by Feenstra et al. [2006] had a familial cryptic duplication of terminal 22q due to der(21)t(21;22)(p10;q13.3), and had very mild manifestations. A recent large-scale study of subtelomere FISH analysis found five patients with terminal 22q duplication that was associated with deletions of other chromosomes [Ravnan et al., 2006]. However, dysmorphic features were not described in their report. Barajas-Barajas et al. [2004] reported two patients with a distal 22q duplication derived from inv(22)(p13q12) in a parent. Distal trisomy 22q detected by conventional chromosome analysis has also been described in more than 15 patients [Barajas-Barajas et al., 2004]. Their clinical manifestations were severe mental and growth retardation, failure to thrive, congenital hypotonia, hydrocephalus, microcephaly, epicanthic folds, low-set ears, broad prominent nasal bridge, long philtrum, cleft palate, micrognathia, finger-like thumbs, cryptorchidism, sensorineural deafness, and occasional early-death. These severe phenotypes are distinct from the features of our patients with terminal 22q microduplication.

Patient 2 also had a deletion for 17p13.3-pter. *LIS1* region responsible for Miller-Dieker syndrome was conserved. Ravnan et al. [2006] reported four patients with terminal 17p deletion. The features observed among them were DiGeorge/Velocardiofacial syndrome, developmental delay and Williams syndrome. Patient 2 lacked features of DiGeorge/Velocardiofacial syndrome and Williams syndrome. We suppose that her abnormal features were attributable mainly to the duplication of distal 22q and to some extent to the terminal deletion of 17p.

SHANK3 is a multidomain protein localized in the postsynaptic density, interacts with various synaptic molecules, and is predominantly expressed in the spine during synaptogenesis [Sheng and Kim, 2000; Uchino et al., 2006]. Thus, terminal 22q duplication may cause the overexpression of *SHANK3*, resulting in interference of proper synaptic development, such as developmental deficiency and abnormal MRI signals observed in Patient 2. Durand et al. [2007] confirmed that haploinsufficiency of *SHANK3* gene is associated with autism. They also identified a 22qter partial trisomy in a boy with Asperger syndrome. Our report may indicate that overexpression of *SHANK3* do not always cause autism.

In conclusion, we here propose a submicroscopic terminal 22q13-duplication as a clinically recognizable syndrome. This duplication may have remained undetected in many cases. Characteristic craniofacial abnormalities, and growth and developmental deficiencies with or without abnormal MRI are most prominent features suggestive of this syndrome. Therefore, such patients are recommended to undergo FISH analysis with subtelomeric probes, for example, *ARSA*, a control probe for the 22q11.2 deletion syndrome. It remains to be investigated whether neurological abnormalities in other patients with the syndrome are associated with *SHANK3* duplication.

ACKNOWLEDGMENTS

We thank the patients and their families for their contribution to this study. This work was supported in part by Ministry of Education, Culture, Sports, Science and Technology of Japan and Osaka Medical Center and Research Institute for MCH Grant for Promotion of Healthy Mothers and Children.

REFERENCES

Barajas-Barajas LO, Valdez LL, Gonzalez JR, Garcia-Garcia C, Rivera H, Ramirez L. 2004. Sensorineural deafness in two infants: A novel feature in the 22q distal duplication syndrome. Cardinal signs in trisomies 22 subtypes. Genet Counsel 15:167–173.

Bonaglia MC, Giorda R, Borgatti R, Felisari G, Gagliardi C, Selicorni A, Zuffardi O. 2001. Disruption of the ProSAP2 gene in a t(12;22)(q24.1;q13.3) is associated with the 22q13.3 deletion syndrome. Am J Hum Genet 69:261–268.

Durand CM, Betancur C, Boeckers TM, Bockmann J, Chaste P, Fauchereau F, Nygren G, Rastam M, Gillberg IC, Anckarsater H, Sponheim E, Goubran-Botros H, Delorme R, Chabane N, Mouren-Simeoni MC, de Mas P, Bieth E, Roge B, Heron D, Burglen L, Gillberg C, Leboyer M, Bourgeron T. 2007. Mutations in the gene encoding the synaptic scaffolding protein SHANK3 are associated with autism spectrum disorders. Nat Genet 39:25–27.

Feenstra I, Koolen DA, Van der Pas J, Hamel BC, Mieloo H, Smeets DF, Van Ravenswaaij CM. 2006. Cryptic duplication of the distal segment of 22q due to a translocation (21;22): Three case reports and a review of the literature. Eur J Med Genet 49:384–395.

Hayashi S, Kurosawa K, Imoto I, Mizutani S, Inazawa J. 2005. Detection of cryptic chromosome aberrations in a patient with a balanced t(1;9)(p34.2;p24) by array-based comparative genomic hybridization. Am J Med Genet Part A 139A:32–36.

Inazawa J, Inoue J, Imoto I. 2004. Comparative genomic hybridization (CGH)-arrays pave the way for identification of novel cancer-related genes. Cancer Sci 95:559–563.

Koolen DA, Reardon W, Rosser EM, Lacombe D, Hurst JA, Law CJ, Bongers EM, van Ravenswaaij-Arts CM, Leisink MA, van Kessel AG, Veltman JA, de Vries BB. 2005. Molecular characterization of patients with subtelomeric 22q abnormalities using chromosome specific array-based comparative genomic hybridization. Eur J Hum Genet 13:1019–1024.

Manning MA, Cassidy SB, Clericuzio C, Cherry AM, Schwartz S, Hudgins L, Enns GM, Hoyme HE. 2004. Terminal 22q deletion syndrome: A newly recognized cause of speech and language disability in the autism spectrum. Pediatrics 114:451–457.

Phelan MC, Rogers RC, Saul RA, Stapleton GA, Sweet K, McDermid H, Shaw SR, Claytor J, Willis J, Kelly DP. 2001. 22q13 deletion syndrome. Am J Med Genet 101:91–99.

Ravnan JB, Tepperberg JH, Papenhausen P, Lamb AN, Hedrick J, Eash D, Ledbetter DH, Martin CL. 2006. Subtelomere FISH analysis of 11 688 cases: An evaluation of the frequency and pattern of subtelomere rearrangements in individuals with developmental disabilities. J Med Genet 43:478–489.

Sheng M, Kim E. 2000. The Shank family of scaffold proteins. J Cell Sci 113:1851–1856.

Uchino S, Wada H, Honda S, Nakamura Y, Ondo Y, Uchiyama T, Tsutsumi M, Suzuki E, Hirasawa T, Kohsaka S. 2006. Direct interaction of post-synaptic density-95/Dlg/ZO-1 domain-containing synaptic molecule Shank3 with GluR1 alpha-amino-3-hydroxy-5-methyl-4-isoxazole propionic acid receptor. J Neurochem 97:1203–1214.

Wilson HL, Wong AC, Shaw SR, Tse WY, Stapleton GA, Phelan MC, Hu S, Marshall J, McDermid HE. 2003. Molecular characterization of the 22q13 deletion syndrome supports the role of haploinsufficiency of SHANK3/PROSAP2 in the major neurological symptoms. J Med Genet 40:575–584.

Direct measurement of protein dynamics inside cells using a rationally designed photoconvertible protein

Tomoki Matsuda[1], Atsushi Miyawaki[2] & Takeharu Nagai[1]

All biological reactions depend on the diffusion and re-localization of biomolecules. Our understanding of biological processes requires accurate measurement of biomolecule mobility in living cells. Currently, approaches for investigating the mobility of biomolecules are generally restricted to measuring either fast or slow diffusion kinetics. We describe the development and application of a photoconvertible fluorescent protein, Phamret, that can be highlighted by UV light stimulation inducing a change in fluorescence emission from cyan fluorescent protein (CFP) to photoactivated GFP (PA-GFP). Phamret can be monitored by single excitation-dual emission mode for visualization of molecular dynamics for a broad range of kinetics. We also devised a microscopy-based method to measure the diffusion coefficient from the fluorescence decay after photostimulation of Phamret, enabling analysis of diffusion kinetics ranging from less than 0.1 $\mu m^2/s$ up to $\sim$100 $\mu m^2/s$, and found significant changes in free protein movement during cell-cycle progression.

Application of GFP and related fluorescent proteins has revolutionized our ability to analyze a wide range of biological processes such as gene expression, protein localization and cell motility in living specimens. Advances in fluorescence microscopy techniques have also enabled higher-resolution imaging of the fluorescence signals from fluorescent protein fusion constructs, providing insights into the movement of biomolecules and their interactions with cellular components[1,2].

Among these methods, imaging fluorescence resonance energy transfer (FRET) between two fluorescent proteins provides spatiotemporal information of protein-protein interactions and protein conformational changes in living cells[3]. FRET is the radiation-less energy transfer from an excited donor to an acceptor fluorophore that occurs when both molecules are in close proximity within $\sim$10 nm at an appropriate orientation of the dipole moment. This technology has been used to develop genetically encoded fluorescent indicators for various cellular events[3].

Several microscopy techniques, including fluorescence correlation spectroscopy (FCS) and fluorescence recovery after photobleaching (FRAP), are used to investigate mobility of biomolecules in living cells. FCS is used to determine the diffusion coefficient and the concentration of biomolecules in live cells by monitoring fluctuations in fluorescence intensity in a diffraction-limited spot of a laser beam[4]. FRAP is also used to investigate protein dynamics by photobleaching fluorescent molecules using a high-powered laser and then recording the movement of surrounding non-bleached fluorescent molecules into the photobleached area[5]. From the recovery curve, it is possible to estimate both the diffusion coefficient and immobile fraction of the tested proteins[6].

In recent years, various photosensitive fluorescent proteins have been developed by engineering existing fluorescent proteins or cloning new proteins from fluorescent organisms[7]. These photosensitive fluorescent proteins provide means to optically highlight selected proteins and to measure protein dynamics. Photosensitive fluorescent proteins can be classified into two types: photoactivatable and photoconvertible fluorescent proteins. Photoactivatable fluorescent proteins are those that are reversibly or irreversibly changed from a dark state to a bright state by photostimulation, such as PA-GFP[8], photoactivatable mRFP1 (ref. 9), KFP1 (ref. 10) and Dronpa[11]. In contrast, photoconvertible fluorescent proteins maintain a bright state but undergo an emission wavelength change from the pre- to post-photoconversion state by photostimulation. Examples of photoconvertible fluorescent proteins are Kaede[12], mEosFP[13], PS-CFP[14], KikGR[15] and Dendra[16]. The ability to detect both pre- and post-photoconversion states is a preferred characteristic for live-cell imaging, but all presently available photoconvertible fluorescent proteins undergo a change in excitation wavelength in addition to the shift in emission wavelength. This therefore requires a complicated microscope setup and also makes it difficult to measure rapid molecular dynamics. Furthermore, photoconvertible fluorescent proteins except PS-CFP, mEosFP and Dendra function as oligomers, which hinders their use as protein tags.

To overcome these problems, we rationally designed a monomeric photoconvertible fluorescent protein, Phamret, that requires only one wavelength to excite both the pre- and post-photoconverted states, thus enabling quantitative observation of rapidly diffusible molecules. We also developed a microscopy method, FDAP, for measurement of rapid diffusion of molecules, up to $\sim$100 $\mu m^2/s$ using Phamret or other photosensitive

[1]Laboratory for Nanosystems Physiology, Research Institute for Electronic Science, Hokkaido University, Kita-12 Nishi-6 Kita-ku, Sapporo, Hokkaido, 060-0812, Japan. [2]Laboratory for Cell Function and Dynamics, Brain Science Institute, RIKEN, 2-1 Hirosawa, Wako, Saitama, 351-0198, Japan. Correspondence should be addressed to T.N. (tnagai@es.hokudai.ac.jp).

RECEIVED 2 JANUARY; ACCEPTED 14 FEBRUARY; PUBLISHED ONLINE 16 MARCH 2008; DOI:10.1038/NMETH.1193

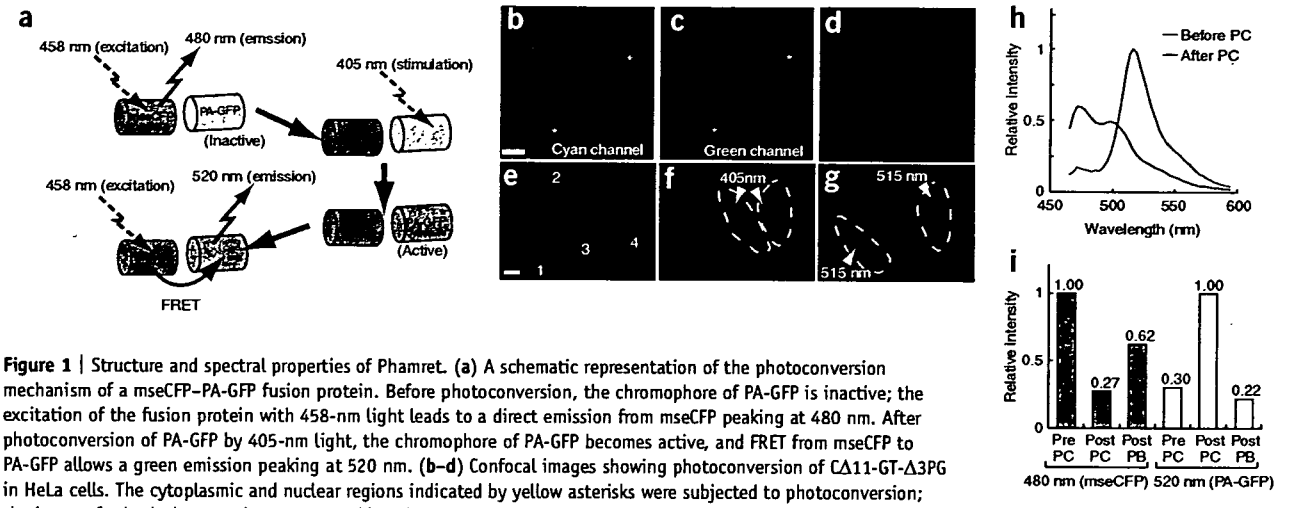

Figure 1 | Structure and spectral properties of Phamret. **(a)** A schematic representation of the photoconversion mechanism of a mseCFP–PA-GFP fusion protein. Before photoconversion, the chromophore of PA-GFP is inactive; the excitation of the fusion protein with 458-nm light leads to a direct emission from mseCFP peaking at 480 nm. After photoconversion of PA-GFP by 405-nm light, the chromophore of PA-GFP becomes active, and FRET from mseCFP to PA-GFP allows a green emission peaking at 520 nm. **(b–d)** Confocal images showing photoconversion of CΔ11-GT-Δ3PG in HeLa cells. The cytoplasmic and nuclear regions indicated by yellow asterisks were subjected to photoconversion; the images for both the cyan (465–510 nm; **b**) and green (510–600 nm; **c**) fluorescence were taken. The images of mseCFP and PA-GFP were pseudocolored (cyan and red, respectively) and superimposed (**d**). **(e–g)** Pseudocolored images of CΔ11-GT-Δ3PG–expressing HeLa cells before photoconversion (**e**), after photoconversion (**f**) and after photobleaching (**g**). The regions surrounded by dashed yellow circles in **f** and **g** were photoconverted by 405-nm light stimulation and photobleached by 515-nm intense laser irradiation, respectively. Scale bars, 10 μm. **(h)** Emission spectra of Phamret in HeLa cells before and after photoconversion (PC). **(i)** Relative fluorescence intensity of mseCFP and PA-GFP before photoconversion (Pre PC), after photoconversion (Post PC) and after photobleaching (Post PB).

fluorescent proteins. The characteristic features of this method are (i) quick photostimulation time (0.25 ms); (ii) small light energy necessary for photostimulation (<1 W/cm^2 in case of Phamret); (iii) fast acquisition of fluorescence decay (4,100 Hz) by reciprocal line scanning; and (iv) consideration of photobleaching during fluorescence decay measurement.

RESULTS

Design and evaluation of Phamret

To develop a photoconvertible fluorescent protein that can be excited by the same wavelength in both pre- and post-photoconversion states, we designed a fusion protein composed of a CFP variant (mseCFP) fused to a PA-GFP[8] (**Fig. 1a**). We designed this fusion protein to emit cyan fluorescence (480 nm) in the pre-photoconverted state, which can be shifted to green fluorescence (520 nm) by UV light stimulation of PA-GFP into a FRET acceptor for the mseCFP donor (**Fig. 1a**). This approach requires a high FRET efficiency between mseCFP and activated PA-GFP; otherwise no or small changes in fluorescence emission can be observed after UV stimulation. To achieve a high FRET efficiency, we concatenated mseCFP containing a C-terminal 11-amino-acid truncation to PA-GFP with a 3-amino-acid truncation from the N terminus via a dipeptide (Gly-Thr) linker. The bacterially expressed chimeric protein (CΔ11-GT-Δ3PG) exhibited a fivefold increase in the emission ratio (520 nm/480 nm) upon brief photoactivation by 420-nm pulsed laser. When expressed in living mammalian cells, CΔ11-GT-Δ3PG was distributed uniformly in both the cytoplasm and the nuclei (**Fig. 1b–d**). Spectral imaging revealed that all fluorescent cells had an emission spectrum identical to that of mseCFP, whereas upon 405-nm laser stimulation, the fluorescence emission in the stimulated area quickly changed from cyan to green, indicative of complete maturation of both mseCFP and PA-GFP in CΔ11-GT-Δ3PG at 37 °C (**Fig. 1e–g** and **Supplementary Fig. 1a–f** online). Upon activation, green fluorescence increased 3.3-fold, and cyan fluorescence emission decreased 3.7-fold, resulting in an approximately 12.2-fold ratio change between the pre- and post-photoconverted states (**Fig. 1h,i**). To confirm that the photoconversion of CΔ11-GT-Δ3PG was indeed due to FRET from mseCFP to activated PA-GFP, we bleached the acceptor PA-GFP. The decrease in PA-GFP emission peak was accompanied by dequenching of the mseCFP signal (**Fig. 1g–i** and **Supplementary Fig. 1g–i**), demonstrating that the dominant mechanism of the fluorescence color change in CΔ11-GT-Δ3PG was caused by FRET between mseCFP and activated PA-GFP. Therefore, we named this fusion protein Phamret for photoactivation-mediated resonance energy transfer. The photoconversion of Phamret was achieved using a lower laser power density (<1 W/cm^2) than that for photobleaching. Accordingly, the quantum yield for photoconversion of Phamret was 2.7×10^{-2}, which was five times greater than that for the efficient highlighter, KikGR[15] (4.7×10^{-3}). pH titration of Phamret revealed that a high dynamic range (>10-fold) was achieved in a neutral to alkaline environment ($>$pH 7), but it was strongly attenuated at acidic pH (**Supplementary Fig. 2a** online) and displayed a twofold dynamic range at pH 6.5. Phamret thus functions as a highlighter at physiological pH ranging from 6.5 to 8.0. Phamret was estimated to be a 53.4-kDa protein and is monomeric in living cells without displaying any unexpected binding to protein or proteolytic digestion (**Supplementary Fig. 2b–d**). Concordantly, Phamret in fusion with human β-actin and fibrillarin as well as targeting sequences for the Golgi bodies and the peroxisome showed an expected localization pattern (**Fig. 2a–d**) as reported previously[17–20]. In addition, the fusion proteins did not substantially perturb cellular functions such as cell division. Furthermore, all the fusion proteins tested underwent pronounced photoconversion by 405-nm laser illumination (**Fig. 2a–d**). Although we successfully labeled most of the proteins tested with Phamret, labeling of α-tubulin was unsuccessful (data not shown). Optimization of the amino-acid linker sequence and length between Phamret

and the protein of interest may resolve this problem. The properties of Phamret in comparison with other photoconvertible fluorescent proteins developed so far are shown in **Table 1**.

Cellular application of Phamret

To demonstrate the applicability of Phamret to stably label the intracellular structures, we expressed Phamret in mitochondria and took time-lapse images after Phamret photoconversion in one region. During a 15-min recording, a long thread-like mitochondrion fused and divided frequently, dramatically changing the pattern of the mitochondria network (**Fig. 2e–h** and **Supplementary Video 1** online). In parallel with the changes in the mitochondria structure, the shifted fluorescence color in the photoconverted region spread out and entered a surrounding mitochondrion. In addition, the labeled region in the fused mitochondrion was exchanged until it came to equilibrium at the intermediate color, indicating conjugation of the mitochondrial matrix and diffusion of the material in the fused mitochondrion.

We also observed positioning of chromosomes during mitosis in living mammalian cells. We labeled chromosomes in HeLa cells by expressing a histone 2B–Phamret fusion protein (H2B-Phamret). Owing to the very low dissociation rate of H2B from chromatin[21], the photoconverted marking remained detectable for many hours, allowing imaging of the dynamics of labeled chromosomes[22]. Just before mitosis, we photoconverted the nuclear halves and performed time-lapse imaging. In most cells (82%, $n = 14$), the global pattern of the mother cells was transmitted to the two daughter nuclei in G1 phase in a mirror-symmetric fashion (**Fig. 2i,j** and **Supplementary Video 2** online), indicating the heritability of chromosomal positions during cell division as previously shown by FRAP analysis using fluorescent protein tags in normal rat kidney cells[22].

Visualization of rapid protein dynamics using Phamret

All photoconvertible fluorescent proteins described to date undergo a change in excitation wavelength in addition to the shift in

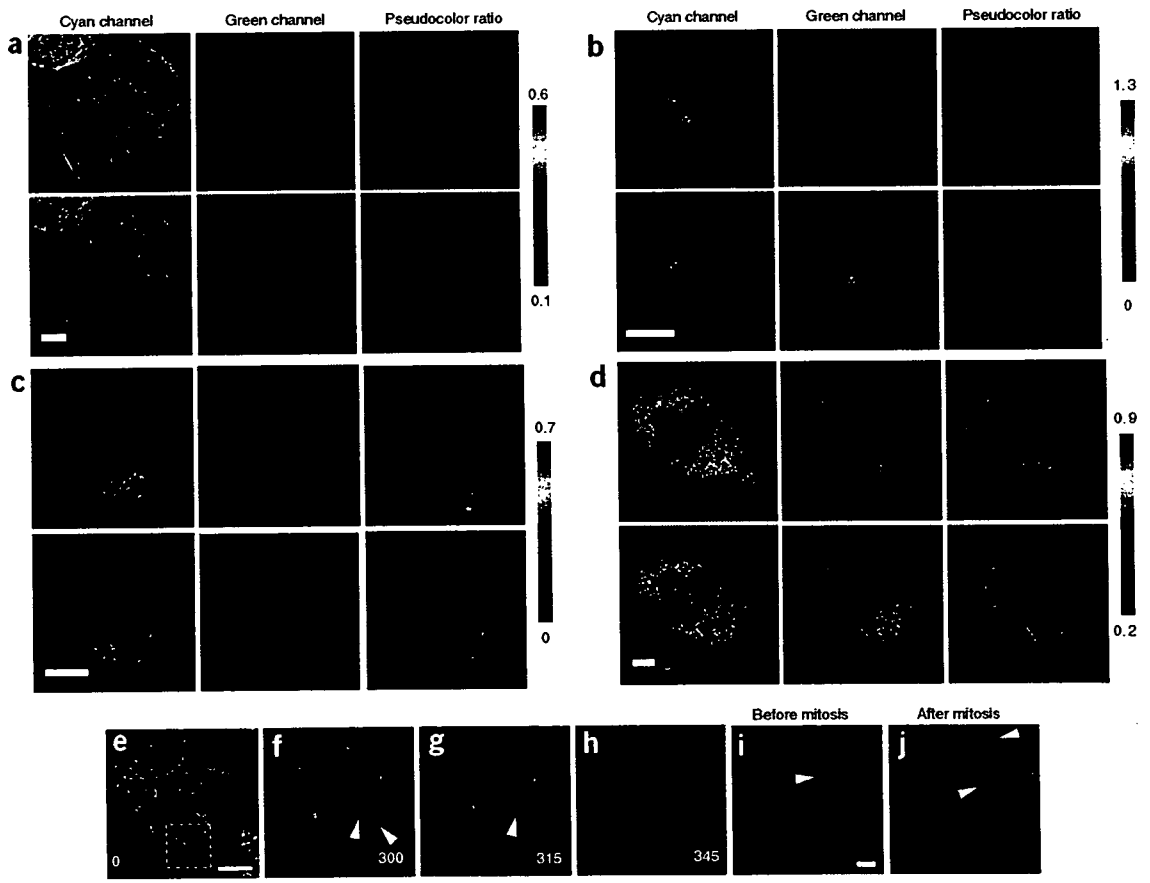

Figure 2 | Photoconversion of Phamret fusion protein in living cells. (**a–d**) Confocal fluorescence images of HeLa cells expressing Phamret fused to actin (**a**), fibrillarin (**b**), Golgi body localizing signal (**c**) and SKL tripeptide for peroxisome localization (**d**) before photoconversion (top) and after photoconversion (bottom) in the selected area, as shown in red (bottom right). The cyan channel, green channel and pseudocolored emission ratio (green to cyan) images are shown. Color bars represent green-to-cyan intensity ratio. (**e–h**) To track mitochondria, Phamret-expressing mitochondria in the selected area (as shown in red in **e**) were subjected to photoconversion (**e**). A yellow dashed box in **e** shows the region used for time-lapse imaging. Representative images taken at 300 s (**f**), 315 s (**g**) and 345 s (**h**) after photoconversion are shown. The yellow and white arrowheads in **f** indicate two mitochondria that were about to fuse. Arrowhead in **g** indicates the point of mitochondrial fusion, which was followed by spreading of Phamret protein in the fused mitochondrion (**h**). (**i,j**) Tracking of H2B-Phamret during mitosis. Half of the nucleus (arrowhead) being photoconverted just before mitosis (red; **i**). The daughter nuclei (arrowheads) show the preserved color pattern (**j**). Scale bars, 10 μm.

Table 1 | Properties of known photoconvertible proteins

Protein	Fluorescence color: Before photoconversion	Fluorescence color: After photoconversion	Observed wavelength[a] (nm): Excitation	Observed wavelength[a] (nm): Emission	Stimulation: Wavelength (nm)	Stimulation: Power density (W/cm^2)	Fluorescence increase in ratio	Oligomeric status	Ref.
Phamret	Cyan	Green	458	475	405	<1[b] ($\Phi_{PC} = 2.7 \times 10^{-2}$)[b]	~15[b]	Monomer	
			458	517					
PS-CFP	Cyan	Green	435	468	405	5–10	~1,500	Monomer	14
			490	511					
Kaede	Green	Red	488	518	405	1.3	~2,000	Tetramer	12
			543	580					
KikGR	Green	Red	488	517	405	~1 ($\Phi_{PC} = 4.7 \times 10^{-3}$)	NS	Tetramer	15
			543	593					
EosFP	Green	Red	488	516	405	NS	NS	Tetramer	13
			543	581					
d2EosFP	Green	Red	488	516	405	500	NS	Dimer	13
			543	581					
mEosFP	Green	Red	488	516	405	NS	NS	Monomer	13
			543	581					
Dendra	Green	Red	488	505	488	1.5	~1,500–4,500	Monomer	16
			543	575	405	0.6			
Cy11.5	Yellow	Cyan	440	527	515 (bleaching)	>10[b]	NS	Monomer	28
			440	476					

Φ_{PC}, quantum yield for photoconversion. NS, not stated.
[a]Wavelength of excitation light for live imaging by microscopy and peak of emission spectrum. [b]Measured in our laboratory. A laser power meter was used to measure total power of the light after the objective lens. Light power density was estimated by dividing the total power by the area of the illuminated region.

emission wavelength upon photoconversion, and thus require measurement in dual excitation–dual emission mode. Generally, two different excitation wavelengths are alternated to obtain images both before and after photoconversion. This is unfavorable for observing rapidly diffusing molecules because of the acquisition time lag between two images. Even if we excite simultaneously the two states of photoconvertible fluorescent proteins, it is impractical because two lasers must be aligned to the same confocal spot by bringing two laser beams to a perfect and stable overlap. The single excitation property of Phamret overcomes this problem, but it may be possible to measure the presently available dual-excitation photoconvertible fluorescent proteins in single-excitation mode also. To address this, we compared the photoconversion contrast of Phamret with the dual-excitation photoconvertible fluorescent proteins, tandem dimer Dendra (td-Dendra), which is comparable in size to Phamret[16]. We expressed both proteins in HeLa cells, photoconverted them by 405-nm laser irradiation and simultaneously measured the change in fluorescence intensity of both pre- and post-photoconversion states at the frame rate of 41 Hz using an appropriate excitation wavelength for each. At the first frame image after photoconversion, Phamret showed a 1.3-fold decrease and 2.4-fold increase in cyan and green fluorescence, respectively, yielding a 3.1-fold change in the emission ratio (**Supplementary Fig. 3a** online). The slower decrease in green fluorescence may be due to the photobleaching of PA-GFP moiety in Phamret. In contrast, td-Dendra had a 1.4-fold decrease in green fluorescence and no change in red fluorescence just after photoconversion, resulting in smaller contrast than for Phamret (**Supplementary Fig. 3b**). These results indicate that when using the single excitation–dual emission mode for fast frame acquisition, Phamret promises a higher contrast than Dendra. To further evaluate this,

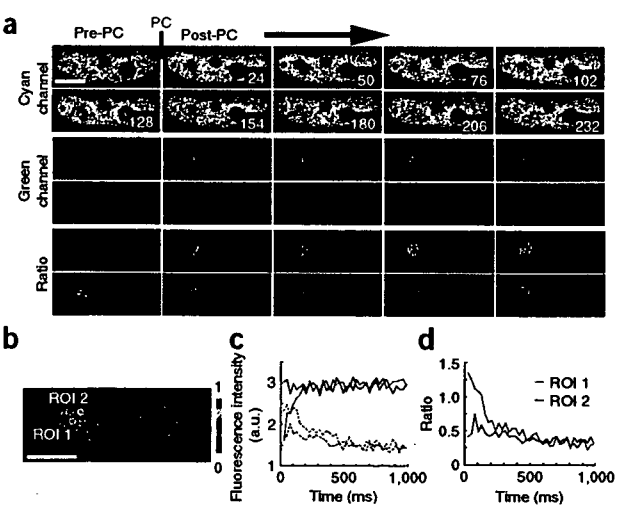

Figure 3 | Visualization of rapid protein dynamics using Phamret. (**a**) Confocal images of donor CFP (top), acceptor PA-GFP (middle) and pseudocolored emission ratio (green/cyan; bottom) showing diffusion of photoconverted PP2Cγ-Phamret. Images were taken every 26 ms. (**b**) A magnified view of the first image just after photoconversion. The white circles (diameter 1.10 μm) represent ROIs used for intensity calculation. ROI 1 was set on the photoconverted circular region (diameter 1.38 μm). ROI 2 was placed outside of the photoconverted region. Distance between the centers of two ROIs is 2.1 μm. (**c**) Time course of cyan (solid line) and green (dashed line) fluorescence intensity of Phamret in ROI 1 (red) and ROI 2 (blue). (**d**) Time course of green to cyan emission ratio in ROI 1 and ROI 2. Scale bars, 10 μm.

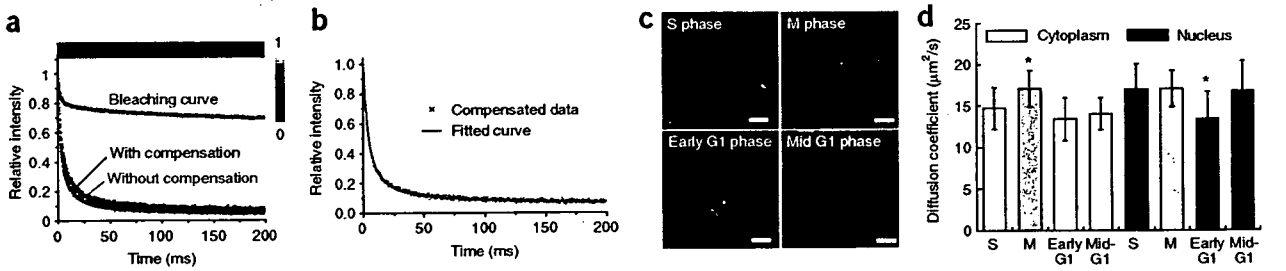

Figure 4 | Determination of diffusion coefficient of Phamret by FDAP. (**a**) Line-scanned images of photoconverted Phamret in solution were taken, and the kymographs of the images are shown in pseudocolor (top). Color bar indicates normalized fluorescence intensity. Average fluorescence decay curves in the solution were calculated (bottom). The blue curve represents the bleaching of photoconverted Phamret during image acquisition. (**b**) The compensated fluorescence decay curve determined by equation (3). (**c**) Fluorescence images of a cell at the indicated cell-cycle stages used for FDAP measurements. Scale bar, 10 μm. (**d**) Diffusion coefficient of Phamret in the cytoplasm and the nucleus at the indicated cell-cycle stages. In the case of M phase, the same data are shown (light gray bars) because the cytoplasm and nucleus cannot be distinguished due to the disappearance of the nuclear membrane. Asterisks (*) indicate the cell phase where the diffusion coefficient is significantly different from other phases in either the cytoplasm or nucleus, respectively. Error bars are s.d. ($n > 10$). Validity of the differences was statistically confirmed by one-way analysis of variance (ANOVA) and defined as significant at $P = 4.0 \times 10^{-6}$ and 4.1×10^{-4}, respectively. Differences between cytoplasm and nucleus in S and G1 phase were also confirmed by using two-sided *t*-test ($P = 0.005$ and 0.008) with significance level $\alpha = 0.05$.

we examined a PP2Cγ-Phamret fusion protein in the nucleus of a HeLa cell. After photoconversion of PP2Cγ-Phamret in a region of the nucleus, we acquired fluorescence images at 41 Hz that show how fast the photoconverted PP2Cγ-Phamret diffuses (**Fig. 3** and **Supplementary Video 3** online).

Determination of biomolecule diffusion coefficients

To determine diffusion coefficients of proteins tagged with photosensitive fluorescent proteins, we devised a new microscopy technique that enables measurement of a wide range of diffusion coefficients. This technique, FDAP, is based on measurement of fluorescence decay after photostimulation of photosensitive fluorescent proteins by quick (0.25 ms) photo-irradiation using a focused laser followed by repeated reciprocal line scanning at 4,100 Hz. We used a laser confocal microscope equipped with a dual laser scanner to carry out photostimulation during fluorescence measurement. We used Phamret as the photosensitive fluorescent protein, and measured the diffusion coefficient in aqueous solution (**Fig. 4a**). When we used averaged fluorescence decay data derived from 10 measurements directly for fitting by Eq. 3, the estimated diffusion coefficient was 70.4 ± 0.8 μm²/s. This value is much larger than 50.4 μm²/s determined by FCS for the GFP tandem dimer[23]. Because the FDAP experiment required about ten times more intense laser irradiation for excitation than that used in FRAP to acquire line images with a high-enough signal-to-noise ratio, we speculated that the difference in measured diffusion coefficients was due to photobleaching of PA-GFP moiety in Phamret during the fluorescence decay measurement (**Supplementary Fig. 3a**). To estimate the influence from photobleaching, we recorded a time course of fluorescence intensity using fully photoconverted Phamret in solution or in a cell in which we neglected the fluorescence decay caused by the molecular diffusion. Although the fluorescence attenuation rate in FDAP was larger than that expected from simple bleaching immediately after starting the measurement, the total number of bleached molecules was comparable between FDAP and FRAP at the end of measurements (**Supplementary Fig. 4a,b** online). We used the measured decay curve (**Fig. 4a**) for data compensation and applied the compensated data for nonlinear curve fitting (**Fig. 4b**). The diffusion coefficient after correction was 49.5 ± 0.6 μm²/s, which was almost equivalent to the previous FCS data[23]. Recently, a method to measure faster diffusion using FRAP by attempting to account for the finite time of the photobleaching has been proposed[24]. Therefore, we performed FRAP measurements to compare the results with those of FDAP (**Supplementary Fig. 4c–f**) and FCS analyses. All three methods gave comparable results for tandem fluorescent protein dimers (**Table 2**). However, the diffusion coefficient of a single fluorescent protein measured by FRAP was substantially different from those obtained by FDAP and FCS, indicating that FDAP may be more reliable than FRAP for analysis of fast-diffusing molecules with >20 μm²/s diffusion coefficient, provided that an accurate bleaching curve can be obtained for correction of the FDAP data (**Table 2**).

To validate the performance of FDAP, we compared the diffusion coefficient of Phamret in HeLa cells at different stages of the cell cycle (S/G2, M, early G1 and mid-G1) as well as in different compartments, cytoplasm and nucleus (**Fig. 4c**). We obtained a correction curve for this experiment using fully photoconverted Phamret in HeLa cells. Generally, the diffusion coefficient of Phamret in the nucleus was greater than that in cytoplasm except in early-G1 phase in which Phamret in both nucleus and cytoplasm showed a similar diffusion coefficient (**Fig. 4d**). Furthermore, we found that the diffusion coefficients in the nucleus during early-G1 phase (13.4 ± 3.3 μm²/s) were significantly smaller than those in other phases (17.0 ± 3.1 in S phase, 17.1 ± 2.2 in M phase, 16.8 ± 3.7 in mid-G1 phase; **Fig. 4d**). Although the cells in M phase are classified into neither cytoplasm nor nucleus because both compartments are mixed after disappearance of the nuclear membrane, the diffusion coefficient of Phamret in M phase tends to show the

Table 2 | Comparison of FDAP with other methods

Fluorescent protein	FDAP D (μm²/s)	FRAP D (μm²/s)	FCS D (μm²/s)
Single	22.9 ± 3.7	34.0 ± 8.5	23.4 ± 2.5
Tandem dimer	14.1 ± 2.4	18.3 ± 6.4	16.4 ± 0.8

value for S and mid-G1 phase nucleus, suggesting that the cellular environment of the M-phase cell was more nuclear-like than cytoplasm-like.

DISCUSSION

The microscopy method we developed, FDAP, allowed reliable measurement of diffusion coefficients up to ~100 μm²/s, the measurement of which has been quite difficult using FRAP. The reason why FRAP gave a different diffusion coefficient in the comparison of FDAP and FCS, may be due to the use of the first frame image after photobleaching to calculate the bleaching constant in FRAP[24]. The first frame image after photobleaching contains irrelevant diffusion data obtained during the photobleaching and the first image acquisition. Thus, this may affect the calculation of the bleaching constant, especially for fast-diffusing molecules, resulting in an overestimation of the diffusion coefficient. According to reference 25, the total bleaching time should be at least 15 times smaller than the characteristic recovery time[25]. The photostimulation time of 0.25 ms in our FDAP measurement is brief enough that the diffusion during photostimulation can be neglected. Moreover, the FRAP measurement has other drawbacks: the bleaching constant needs to be determined whenever the target molecules or intracellular environment are changed because the value of the bleaching constant depends on the diffusion constant of the target molecules. In the presence of a highly immobile fraction, the bleaching profile in the first image contains contributions of both the diffusing mobile fraction and the stationary immobile fraction, requiring complex assumptions[24]. Our FDAP method is not affected by this issue.

Compared to FCS, FDAP has the advantage of retrieving additional information regarding the states of the immobile molecules. FDAP can be used to investigate any diffusion kinetics ranging from <0.1 μm²/s to ~100 μm²/s. Notably, when compared with FCS, measurement time for a fast diffusible protein (>10 μm²/s) by FDAP is much shorter (200 ms for FDAP versus >10 s FCS[23]), which is an advantage when analyzing molecules that quickly change diffusion coefficient upon stimulation.

In the post genomic era, many cascade maps for signal transduction pathways activated by biological events have been described. These maps are very useful for understanding the mechanisms of cellular activity at the molecular level. Information on protein and molecule movement rates within cells provides enhanced understanding of not only signal transduction but also various physiological phenomena at the molecular level. The ability to measure molecular mobility over a broad kinetic range with this single technique provides a useful complement to FRAP or FCS, thus benefiting studies on molecular dynamics in living cells.

METHODS

Imaging. For cell imaging we used an Olympus confocal inverted microscope FV1000 equipped with UPLSAPO 60× 1.35 numerical aperture (NA) oil objective and multi-Argon ion laser. We used a 405 nm laser diode for photostimulation. We acquired the cyan and green fluorescence signals by excitation at 458 nm and detected them at 465–510 nm and 510–600 nm wavelength range, respectively. For td-Dendra imaging, we simultaneously acquired the green (495–525 nm) and red fluorescence (560–650 nm) signals by excitation at 488 nm. We created the fluorescence ratio images using AquaCosmos software (Hamamatsu Photonics).

Determination of diffusion coefficient by FDAP. We estimated the activation characteristics of the laser using fixed cells expressing Phamret. First, we photoconverted Phamret in a fixed cell by the pulse irradiation with a 405-nm laser for 0.25 ms, and measured fluorescence intensity. Then we photoconverted the whole region of the same cell again until the fluorescence came to equilibrium, and again measured the fluorescence intensity. We divided the fluorescence intensity of once-photoconverted Phamret at the position (r) from the center of the activated region by the fluorescence intensity of fully photoconverted Phamret. We fitted the divided values at different positions to the Gaussian laser profile modified from the previously published one[26] so that the center of the activation profile became the peak value of fluorescence intensity as described by following equation:

$$C(r) = 1 - \exp\left(-K\exp\left(-\frac{2r^2}{w^2}\right)\right), \quad (1)$$

where $C(r)$ is the concentration of the photoconverted Phamret, K is the activation constant for the fixed cells, and w is the half-width of the laser beam at $1/e^2$ intensity.

Each FDAP experiment started with image scans, followed by a 405-nm laser irradiation for 0.25 ms on a point in the scanning area. We collected a series of line scanned images of the fluorescence emission in the region of 510–600 nm at 0.244 ms intervals (≈4,100 Hz) for 200 ms using 488-nm laser as excitation light. We skipped the first line scanning image to avoid direct influence of the irradiated pulse of the 405 nm laser. We fixed the length of line scanning to 80 pixels, and each pixel width was 103 nm. We used the central 8 pixels (0.824 μm) in the scanned line as a region of interest for the fluorescence intensity measurement. We calculated the background signals as the average intensity in the region of interest, which we measured 50 ms before photoconversion. We calculated the average fluorescence in the region of interest (ROI) at time t after the photoconversion, $I_{ROI}(t)$, from each line image with the subtracted background signal. The fluorescence signal measured in a region of interest normalized to the change in total fluorescence was determined as

$$I_{\text{rel. image}}(t) = \frac{I_{ROI}(t)}{I_{max}}, \quad (2)$$

where I_{max} is the maximum intensity after the photoconversion.

Because the measured fluorescence decay contains contribution from photobleaching, the original fluorescence decay data must be compensated. To do this, we measured a time course of the photobleaching of completely photoconverted Phamret. We then divided the originally acquired decay curve by the photobleaching curve and used the recalculated data for the curve fitting. Using the values of K and w, we fitted the FDAP decay curves of $I_{\text{rel. image}^*}(t)$ to the decay function, $I_{\text{rel. calc.}}(t)$ modified from that reported for FRAP[27]:

$$I_{\text{rel. image}^*}(t) = \alpha \times I_{\text{rel. calc}}(t)$$

$$= \alpha\left(1-\left((1-\beta)\sum_{n=0}^{+\infty}\frac{(-K)^n}{n!}\left(1+n\left(1+\frac{2t}{\tau_D}\right)\right)^{-1}+\beta\frac{1-e^{-K}}{K}\right)\right) \quad (3)$$

where α is a parameter to conform $I_{\text{rel. calc.}}$ to $I_{\text{rel. image}^*}$ at $t = 0$ and β is the fraction of immobile molecules (ranging from 0 to 1).

τ_D is the characteristic diffusion time related to the diffusion coefficient, D, by $\tau_D = w^2/4D$. The series solution for the fluorescence decay was truncated after 40 terms[18], assuring that the neglected terms made an insignificant contribution. All of the curve fittings were done by using a weighted least-squares algorithm implemented in Origin (OriginLab).

Additional methods. The methods for plasmid construction, cell culture and transfections, protein purification, gel filtration, spectroscopy, pH titration, measurement of photoconversion quantum yield and western blotting are available in **Supplementary Methods** online.

Note: Supplementary information is available on the Nature Methods website.

ACKNOWLEDGMENTS

We thank H. Kimura and Y. Yoneda (Osaka University) for providing the cDNA encoding H2B-GFP and PP2Cγ, and fibrillalin, respectively. We also thank D. Goto and I. Kotera for helpful comments. We also thank F. Inagaki and N. Noda for help with gel filtration analysis. This work was partially supported by grants from Scientific Research on Advanced Medical Technology of the Ministry of Labor, Health and Welfare of Japan, Precursory Research for Embryonic Science and Technology of the Japan Science and Technology Agency, and the Japanese Ministry of Education, Science and Technology.

AUTHOR CONTRIBUTIONS

T.M. performed experiments, analyzed data and prepared the manuscript; A.M. contributed to data analysis; T.N. contributed to the conceptual development and experimental design and performed experiments, analyzed data and prepared the manuscript.

Published online at http://www.nature.com/naturemethods/
Reprints and permissions information is available online at http://npg.nature.com/reprintsandpermissions

1. Lippincott-Schwartz, J., Snapp, E. & Kenworthy, A. Studying protein dynamics in living cells. *Nat. Rev. Mol. Cell Biol.* **2**, 444–456 (2001).
2. Zhang, J., Campbell, R.E., Ting, A.Y. & Tsien, R.Y. Creating new fluorescent probes for cell biology. *Nat. Rev. Mol. Cell Biol.* **3**, 906–918 (2002).
3. Miyawaki, A. Visualization of the spatial and temporal dynamics of intracellular signaling. *Dev. Cell* **4**, 295–305 (2003).
4. Medina, M.A. & Schwille, P. Fluorescence correlation spectroscopy for the detection and study of single molecules in biology. *Bioessays* **24**, 758–764 (2002).
5. Reits, E.A. & Neefjes, J.J. From fixed to FRAP: measuring protein mobility and activity in living cells. *Nat. Cell Biol.* **3**, E145–E147 (2001).
6. White, J. & Stelzer, E. Photobleaching GFP reveals protein dynamics inside live cells. *Trends Cell Biol.* **9**, 61–65 (1999).
7. Lukyanov, K.A., Chudakov, D.M., Lukyanov, S. & Verkhusha, V.V. Innovation: Photoactivatable fluorescent proteins. *Nat. Rev. Mol. Cell Biol.* **6**, 885–891 (2005).
8. Patterson, G.H. & Lippincott-Schwartz, J. A photoactivatable GFP for selective photolabeling of proteins and cells. *Science* **297**, 1873–1877 (2002).
9. Verkhusha, V.V. & Sorkin, A. Conversion of the monomeric red fluorescent protein into a photoactivatable probe. *Chem. Biol.* **12**, 279–285 (2005).
10. Chudakov, D.M. *et al.* Kindling fluorescent proteins for precise *in vivo* photolabeling. *Nat. Biotechnol.* **21**, 191–194 (2003).
11. Ando, R., Mizuno, H. & Miyawaki, A. Regulated fast nucleocytoplasmic shuttling observed by reversible protein highlighting. *Science* **306**, 1370–1373 (2004).
12. Ando, R., Hama, H., Yamamoto-Hino, M., Mizuno, H. & Miyawaki, A. An optical marker based on the UV-induced green-to-red photoconversion of a fluorescent protein. *Proc. Natl. Acad. Sci. USA* **99**, 12651–12656 (2002).
13. Wiedenmann, J. *et al.* EosFP, a fluorescent marker protein with UV-inducible green-to-red fluorescence conversion. *Proc. Natl. Acad. Sci. USA* **101**, 15905–15910 (2004).
14. Chudakov, D.M. *et al.* Photoswitchable cyan fluorescent protein for protein tracking. *Nat. Biotechnol.* **22**, 1435–1439 (2004).
15. Tsutsui, H., Karasawa, S., Shimizu, H., Nukina, N. & Miyawaki, A. Semi-rational engineering of a coral fluorescent protein into an efficient highlighter. *EMBO Rep.* **6**, 233–238 (2005).
16. Gurskaya, N.G. *et al.* Engineering of a monomeric green-to-red photoactivatable fluorescent protein induced by blue light. *Nat. Biotechnol.* **24**, 461–465 (2006).
17. Ballestrem, C., Wehrle-Haller, B. & Imhof, B.A. Actin dynamics in living mammalian cells. *J. Cell Sci.* **111**, 1649–1658 (1998).
18. Phair, R.D. & Misteli, T. High mobility of proteins in the mammalian cell nucleus. *Nature* **404**, 604–609 (2000).
19. Llopis, J., McCaffery, J.M., Miyawaki, A., Farquhar, M.G. & Tsien, R.Y. Measurement of cytosolic, mitochondrial, and Golgi pH in single living cells with green fluorescent proteins. *Proc. Natl. Acad. Sci. USA* **95**, 6803–6808 (1998).
20. Recalcati, S., Menotti, E. & Kühn, L.C. Peroxisomal targeting of mammalian hydroxyacid oxidase 1 requires the C-terminal tripeptide SKI. *J. Cell Sci.* **114**, 1625–1629 (2001).
21. Kimura, H. & Cook, P.R. Kinetics of core histones in living human cells: little exchange of H3 and H4 and some rapid exchange of H2B. *J. Cell Biol.* **153**, 1341–1353 (2001).
22. Gerlich, D. *et al.* Global chromosome positions are transmitted through mitosis in mammalian cells. *Cell* **112**, 751–764 (2003).
23. Pack, C., Saito, K., Tamura, M. & Kinjo, M. Microenvironment and effect of energy depletion in the nucleus analyzed by mobility of multiple oligomeric EGFPs. *Biophys. J.* **91**, 3921–3936 (2006).
24. Braga, J., Desterro, J.M.P. & Carmo-Fonseca, M. Intracellular macromolecular mobility measured by fluorescence recovery after photobleaching with confocal laser scanning microscopes. *Mol. Biol. Cell* **15**, 4749–4760 (2004).
25. Meyvis, T.K., De Smedt, S.C., Van Oostveldt, P. & Demeester, J. Fluorescence recovery after photobleaching: a versatile tool for mobility and interaction measurements in pharmaceutical research. *Pharm. Res.* **16**, 1153–1162 (1999).
26. Axelrod, D., Koppel, D.E., Schlessinger, J., Elson, E. & Webb, W.W. Mobility measurement by analysis of fluorescence photobleaching recovery kinetics. *Biophys. J.* **16**, 1055–1069 (1976).
27. Calapez, A. *et al.* The intranuclear mobility of messenger RNA binding proteins is ATP dependent and temperature sensitive. *J. Cell Biol.* **59**, 795–805 (2002).
28. Shimozono, S. *et al.* Concatenation of cyan and yellow fluorescent proteins for efficient resonance energy transfer. *Biochemistry* **45**, 6267–6271 (2006).

Local initiation of caspase activation in *Drosophila* salivary gland programmed cell death *in vivo*

Kiwamu Takemoto*†, Erina Kuranaga*, Ayako Tonoki*, Takeharu Nagai†‡, Atsushi Miyawaki‡, and Masayuki Miura*§

*Department of Genetics, Graduate School of Pharmaceutical Sciences, University of Tokyo, Bunkyo-ku, Tokyo 113-0033, Japan; †Laboratory for NanoSystems Physiology, Research Institute for Electronic Science, Hokkaido University, Kita 12 Nishi 6, Kita-ku, Sapporo 060-0812, Japan; and ‡Laboratory for Cell Function Dynamics, RIKEN Brain Science Institute, 2-1 Hirosawa, Wako, Saitama 351-0198, Japan

Edited by Hermann Steller, The Rockefeller University, New York, NY, and accepted by the Editorial Board July 11, 2007 (received for review March 23, 2007)

Programmed cell death, or apoptosis, is an essential event in animal development. Spatiotemporal analysis of caspase activation *in vivo* could provide new insights into programmed cell death occurring during development. Here, using the FRET-based caspase-3 indicator, SCAT3, we report the results of live-imaging analysis of caspase activation in developing *Drosophila in vivo*. In *Drosophila*, the salivary gland is sculpted by caspase-mediated programmed cell death initiated by the steroid hormone 20-hydroxyecdysone (ecdysone). Using a SCAT3 probe, we observed that caspase activation in the salivary glands begins in the anterior cells and is then propagated to the posterior cells *in vivo*. *In vitro* salivary gland culture experiments indicated that local exposure of ecdysone to the anterior salivary gland reproduces the caspase activation gradient as observed *in vivo*. In *βFTZ-F1* mutants, caspase activation was delayed and occurred in a random pattern *in vivo*. In contrast to the *in vivo* response, the salivary glands from *βFTZ-F1* mutants showed a normal *in vitro* response to ecdysone, suggesting that *βFTZ-F1* may be involved in ecdysteroid biosynthesis and secretion of ecdysone from the ring gland for local initiation of programmed cell death. These results imply a role of *βFTZ-F1* in coordinating the initiation of salivary gland apoptosis in development.

apoptosis | imaging | metamorphosis | FRET | ecdysone

Developmental processes are regulated by many events, including cell proliferation, differentiation, migration, and cell death. Programmed cell death is an essential event in animal development and is important for maintaining animal homeostasis by controlling cell numbers, removing abnormal cells, and sculpting developmental structures in normal morphogenesis.

Steroid hormones regulate many types of biological responses, including programmed cell death during animal development (1). During *Drosophila* metamorphosis, successive pulses of 20-hydroxyecdysone (ecdysone) trigger the differentiation and morphogenesis of the imaginal discs, to give rise to adult tissues, and the programmed cell death of larval cells, to eliminate obsolete tissues (2). An increased ecdysone titer at the end of the third-instar larval phase induces puparium formation and marks the onset of metamorphosis. This ecdysone pulse triggers the programmed cell death of larval mid-gut and anterior muscles. About 12 h after puparium formation (APF), a subsequent ecdysone pulse induces the prepupal–pupal transition. In response to this signal, the head assumes the appropriate position by everting from inside the thorax, and the leg imaginal discs complete their elongation. This increased ecdysone titer also triggers the larval salivary gland to undergo programmed cell death, and the gland regresses completely within 4–6 h after the hormone titer peak (3–5). In this programmed cell death of the salivary gland, ecdysone induces expression of the early genes, *E93*, *E74*, and *BR-C*, which in turn induce the caspase family cell death executors (6, 7). However, the mechanisms involved in regulation of the spatiotemporal specification of metamorphosis-related events, including programmed cell death and caspase activation, are not well understood. The primary goal of the present work was to determine how the spatiotemporal pattern of programmed cell death is coordinated to initiate tissue regression during metamorphosis.

In recent years, many molecules involved in "cell killing" have been identified. Caspases are cysteine proteases that execute cell-killing programs, in which they cleave specific target proteins, resulting in cell degradation. In *Drosophila*, seven caspases (DCP-1, drICE, Dredd, DRONC, Decay, DAMM, and STRICA/Dream) have been identified and shown to be required for the cell death induced by various stimuli (8). These caspases are regulated, in part, by an Apaf-1 homolog, Dark (Dapaf-1/HAC-1). Loss of Dark function leads to reduced apoptosis in the embryo and larval brain (9–11). DRONC and its activator, Dark, are also involved in developmental cell death in various tissues and are required for programmed cell death in the larval salivary gland (12–14). These findings suggest that caspase-mediated pathways are important for programmed cell death *in vivo*. To investigate the spatiotemporal pattern of programmed cell death in developmental tissue regression *in vivo*, we focused on caspase activation in the salivary gland during metamorphosis. Recently, FRET technology has been used to develop genetically encoded fluorescent indicators for various cellular functions, including enzymatic activities and calcium concentrations. We have reported a FRET-based caspase indicator, SCAT3, that reliably provides signals from caspase activity in living cells (15).

Here, using SCAT3, we report direct observations of caspase activation in living *Drosophila*. Using live-imaging analysis during salivary gland programmed cell death, we found that the caspase activation was locally and symmetrically initiated in the anterior cells. The caspase activation then propagated to the posterior cells. The reactivity to ecdysone is similar between salivary cells *in vitro*, but the anterior–posterior pattern of caspase activation in the salivary gland requires local exposure to ecdysone. We also demonstrated that *βFTZ-F1* is required for the spatial pattern of caspase activation in the salivary glands, probably through the regulation of ecdysone biosynthesis and its secretion into the anterior part of the salivary gland.

Results

Local Activation and Propagation of Caspase During Salivary Gland Cell Death. To analyze the spatiotemporal pattern of caspase activation in the pupal salivary gland *in vivo*, a FRET-based caspase indicator, SCAT3, was expressed in the salivary glands with an *N393* driver. Using this driver, SCAT3 expression was obtained from the

Author contributions: K.T., E.K., A.T., and M.M. designed research; K.T., E.K., and A.T. performed research; T.N. and A.M. contributed new reagents/analytic tools; K.T., E.K., A.T., and M.M. analyzed data; and K.T. and M.M. wrote the paper.

The authors declare no conflict of interest.

This article is a PNAS Direct Submission. H.S. is a guest editor invited by the Editorial Board.

Abbreviations: APF, after puparium formation; ecdysone, 20-hydroxyecdysone; ECFP, enhanced cyan fluorescent protein.

§To whom correspondence should be addressed. E-mail: miura@mol.f.u-tokyo.ac.jp.

This article contains supporting information online at www.pnas.org/cgi/content/full/0702733104/DC1.

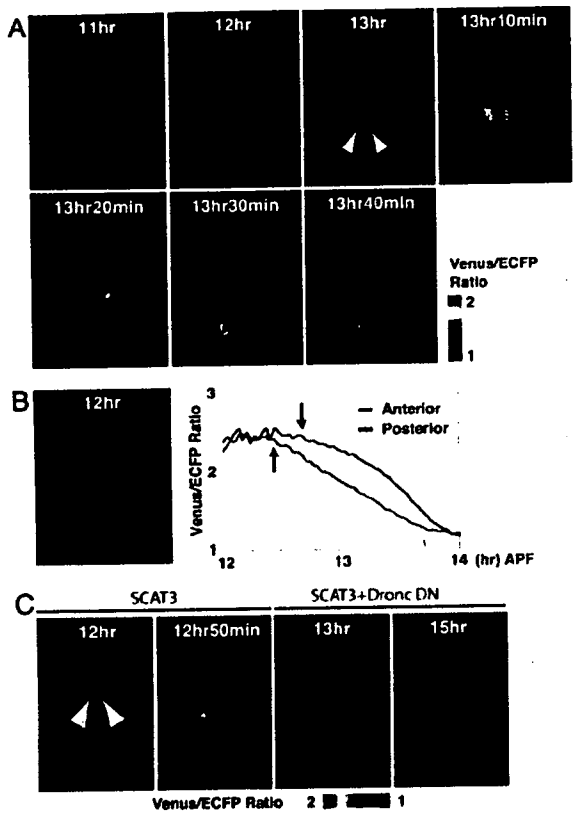

Fig. 1. Local activation and propagation of the caspase activities during programmed cell death in the salivary gland *in vivo*. (*A*) Ratio images of SCAT3-expressing salivary glands. *In vivo* live-imaging analysis of SCAT3 was begun 10–11 h APF. Arrowheads indicate the symmetrical initiation of caspase activation. Time indicates APF. The genotype was *N393/+; UAS-SCAT3/+*. (*B*) FRET ratio reduction was initially observed in the anterior (red line) and then in the posterior region (blue line) in the salivary glands examined in *A*. (*Left*) The region of interest is denoted by a red circle (anterior part) and blue circle (posterior part). (*Right*) Arrows indicate the time at which caspase activation was started. Initiation of caspase activation was determined as the time the ratio was continuously lower than the baseline ratio for 5 min. (*C*) *Dronc* was involved in the spatiotemporal pattern of caspase activation. Time indicates APF. Each arrowhead indicates symmetrical initiation of caspase activation. The indicated genotypes were as follows: *SCAT3* (*sca-Gal4/UAS-SCAT3*), and *SCAT3+Dronc DN* (*sca-Gal4/UAS-SCAT3; UAS-Dronc DN/+*). DN, dominant-negative.

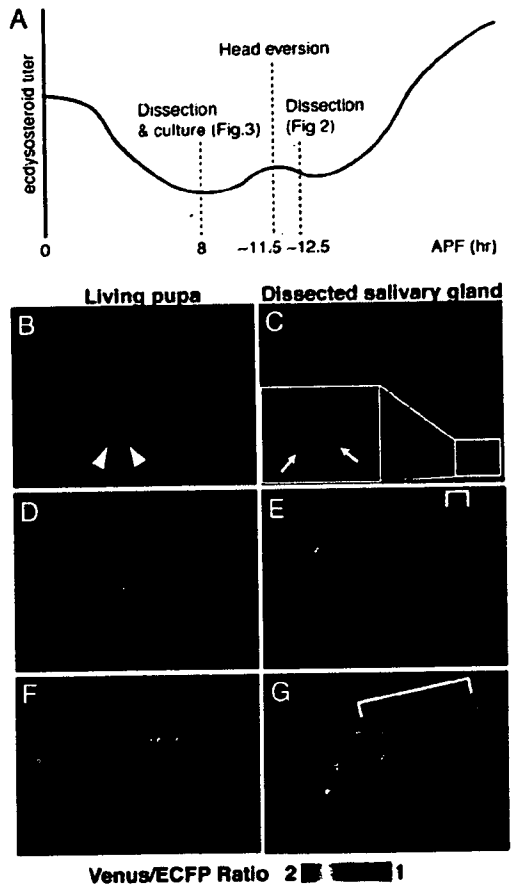

Fig. 2. Local caspase activation starts in anterior cells in the salivary gland. (*A*) Schematic representation of experiments shown in Figs. 2 and 3. The profile of the ecdysone titer is illustrated according to Thummel (29). (*B–G*) The initiation of caspase activation was observed in anterior gland cells. The initiation and propagation of caspase activation were observed in living pupae *in vivo* (*B*, *D*, and *F*). Each salivary gland was dissected from the observed pupa and fixed. Fixed salivary glands were subjected to monitoring for caspase activation *in vitro* (*C*, *E*, and *G*, respectively). The arrows, arrowheads, and white line indicate cells with high caspase activities. The genotype was *N393/+; UAS-SCAT3/+*.

embryonic stage (16). In this system, caspase activation causes a decrease in the FRET signal, resulting in a decrease in the Venus enhanced cyan fluorescent protein (ECFP) emission ratio. We performed this analysis by placing individual living pupae into a glass-bottomed dish and visualizing the caspase activation *in vivo* by time-lapse FRET analysis with wide-field microscopy. In the SCAT3-expressing pupae, adult head eversion occurred at the normal time, 11–12 h APF (11 h 34 min ± 21 min; $n = 10$). At the same time, the large lobes of the salivary glands were rapidly stretched (17). Caspase activation was first detected after head eversion, at 12 h 17 min ± 24 min APF ($n = 10$). We observed that caspase activation was initiated in a restricted region in the anterior of the gland and that this signal then propagated to the posterior salivary cells in the pupae analyzed [Fig. 1 *A* and *B* and supporting information (SI) Movie 1]. The patterns were simultaneous and symmetrical in the right and left salivary glands, along the median line. The maximum caspase activation in the posterior cells was observed 86.4 ± 16.9 min ($n = 10$) after caspase activation began in the anterior cells. The caspase activity-induced reduction in FRET signals was clearly suppressed by expression of a dominant-negative DRONC (Fig. 1*C*), indicating that a DRONC-dependent pathway was involved in generating this pattern. This work represents a direct observation of caspase activation and programmed cell death in living animals *in vivo*.

To determine where caspase activation was initiated at the single-cell level, we isolated salivary glands from pupae at different time points during development and examined caspase activation *in vitro* by confocal microscopy (Fig. 2 *C*, *E*, and *G*). Caspase activities were initiated in only a few cells of the anteriormost part of the salivary glands (two cells in Fig. 2*C*; arrows). When propagation to the posterior region was observed *in vivo* (Fig. 2 *D* and *F*), the progression of caspase activation was clearly observed by *in vitro* confocal microscopy analysis (Fig. 2 *E* and *G* compared with Fig. 2*C*). These results suggested that

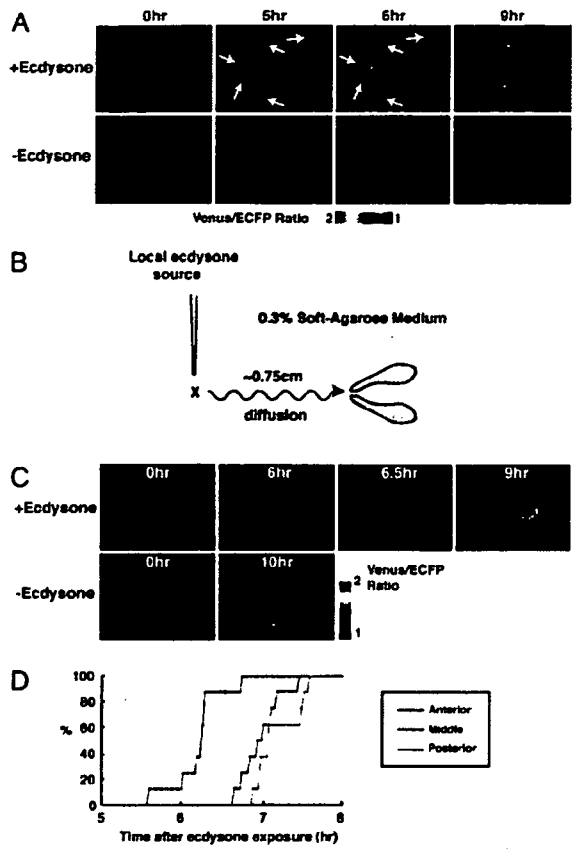

Fig. 3. *In vitro* response of salivary gland to ecdysone. (*A*) Random initiation of caspase activation induced by ecdysone exposure *in vitro*. Salivary glands at 8 h APF were carefully dissected and cultured *in vitro*, and 50 μM ecdysone was added to cultured salivary glands to induce caspase activation. Arrows indicate cells with high caspase activity. The genotype was *N393/+; UAS-SCAT3/+*. (*B–D*) Local initiation and propagation of caspase activation by anterior-localized source of ecdysone. Salivary glands at 8 h APF were carefully dissected and cultured *in vitro* in 0.3% soft agarose-containing medium (2 ml). Then, 1 μl of 50 mM ecdysone or ethanol (control) was added to the anterior part of the salivary gland. The time courses of caspase activation in anterior, middle, and posterior region are plotted in *D* ($n = 8$). The percentage of salivary glands that showed caspase activation in the indicated region was plotted. Caspase activation was determined by a 20% decrease from the basal ratio.

caspase activation was initiated locally in the anterior region and propagated to the posterior region of the salivary gland.

***In Vitro* Response to Ecdysone in Salivary Gland Cells.** Next, we examined whether this pattern of caspase activation occurred specifically *in vivo*. The salivary glands from pupae were isolated at 8 h APF and cultured *in vitro* in culture medium. The salivary glands could be maintained for at least 17 h under these culture conditions (data not shown). Strong caspase activation was observed 6 h after the addition of ecdysone to the salivary glands (Fig. 3*A Upper*). However, the caspase activation was initiated in a random pattern *in vitro* (arrows in Fig. 3*A*), unlike the *in vivo* pattern shown in Figs. 1 and 2. These results suggest that the ability to respond to ecdysone is equal among salivary cells.

We also examined the results of local application of ecdysone in 0.3% soft agarose-containing medium to achieve slow diffusion of ecdysone from anterior to posterior *in vitro* (Fig. 3*B*). Caspase activation was shown to be initiated in the anterior cells and propagated to the posterior cells in the salivary gland by diffusion of ecdysone from the anterior part (Fig. 3*C Upper*). Caspase activation was not observed at least within 10 h in control experiments (Fig. 3*C Lower*). We also plotted the time course of caspase activation in anterior, middle, and posterior regions (Fig. 3*D*), and the results indicated that caspase activation was initiated in anterior cells and propagated to middle and posterior cells. These results suggest that the spatiotemporal pattern of caspase activation in the salivary gland *in vivo* is the result of ecdysone diffusion and transport from the anterior side.

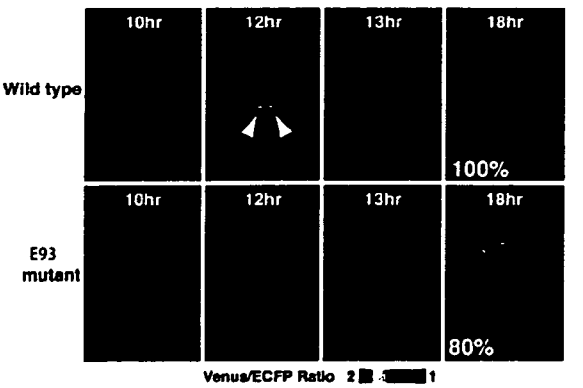

Fig. 4. Defect of caspase activation in *E93* mutants *in vivo*. *In vivo* live imaging was performed on pupae from 10 h APF. Arrowheads indicate the symmetrical initiation of caspase activation in the wild-type control. Numbers indicate the population of flies that showed these phenotypes. The indicated genotypes were: wild-type (*N393/+; UAS-SCAT3/+*) and *E93* mutant [*N393/+; UAS-SCAT3/+; $E93^1$/Df(3R)93F^{2}*].

Defective Caspase Activation in *E93* Mutants. To investigate how the caspase activation pattern was formed and regulated *in vivo*, we used live-imaging analysis of mutants defective in ecdysone-induced genes. It has been reported that flies with mutations in *E93*, *E74A*, *βFTZ-F1*, or *BR-C* show inhibited programmed cell death in the salivary glands (6, 7, 17, 18). In *E93* mutants, late genes, including the *Drosophila* caspases *dronc* and *dark*, showed reduced expression (19), resulting in inhibition of salivary gland cell death. We first examined the *E93* gene mutation with SCAT3 live-imaging analysis (Fig. 4). In all of the *E93* mutants examined, head eversion occurred normally, suggesting that the prepupal pulse of ecdysone was normal. However, our live-imaging analysis showed that caspase activation in these mutants was strongly inhibited, at least within the first 18 h APF (80%; $n = 10$). These results suggested that the *E93* gene is an executor for caspase activation in salivary gland *in vivo*.

Defects in Spatial Regulation of Caspase Activation in *βFTZ-F1* Mutants. We next examined whether the spatial distribution of the ecdysone pulse *in vivo* could be involved in determining the spatial pattern of caspase activation in the salivary gland. Previous studies indicated that *βFTZ-F1* mutants show defective adult head eversion and leg elongation, suggesting that the prepupal pulse of ecdysone is abnormal in these mutants (18). Therefore, we investigated the spatial pattern of caspase activation in a *βFTZ-F1* mutant (Fig. 5). Almost all of the *βFTZ-F1* mutant pupae expressing SCAT3 showed defects in adult head eversion (90%; $n = 21$). The results of live-imaging analysis with SCAT3 *in vivo* indicated complete inhibition of caspase activation in 29% of the *βFTZ-F1* mutants, at least within the first 18 h APF (Fig. 5*A* case 1; $n = 21$). In the other mutants, caspase activation was significantly delayed: decreases in

DEVELOPMENTAL BIOLOGY

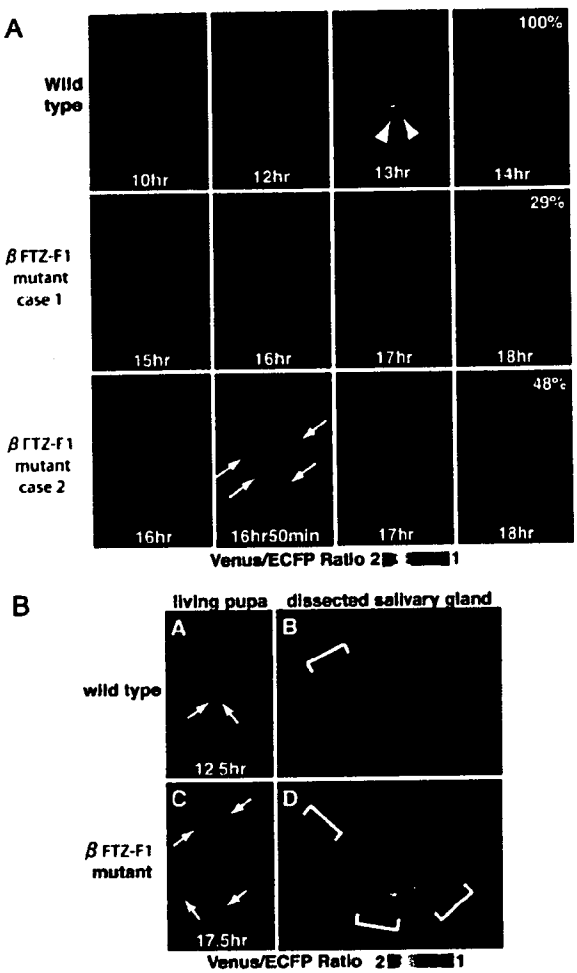

Fig. 5. Defects in adult head eversion and the spatial pattern of caspase activation in *βFTZ-F1* mutants *in vivo*. (*A*) *In vivo* live imaging was performed from 10 h APF in wild-type controls and *βFTZ-F1* mutants. Arrowheads indicate the symmetrical initiation of caspase activation in wild-type controls. Arrows indicate the random initiation of caspase activation in *βFTZ-F1* mutants. Case 1 refers to pupae showing no caspase activation up to 18 h APF. Case 2 refers to the pupae that showed delayed and randomly initiated caspase activation. In case 2, the propagation of caspase activation characteristic of wild-type controls (Fig. 1*A*) was not observed. Numbers indicate the percentages of the population. (*B*) Defect in the spatial pattern of caspase activation in *βFTZ-F1* mutants. The spatial pattern of caspase activation was compared between dissected salivary glands from wild-type controls and *βFTZ-F1* mutants. Once the caspase activation was started as determined by *in vivo* imaging (*A* and *C*, arrows), the salivary gland from the observed pupa was dissected and fixed. Time indicates APF (in hours). The indicated genotypes in this figure are wild-type (*N393/+; UAS-SCAT3/+*) and *βFTZ-F1* mutant (*N393/+; UAS-SCAT3/+; βFTZ-F1^{17}/βFTZ-F1^{19}*).

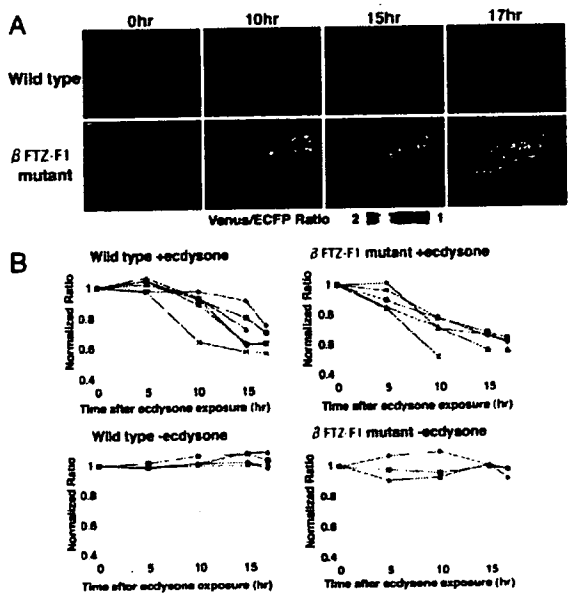

Fig. 6. Normal response to ecdysone in salivary glands isolated from *βFTZ-F1* mutants *in vitro*. (*A*) Caspase activation in *βFTZ-F1* mutants in response to ecdysone. The salivary glands were carefully dissected from wild-type controls or *βFTZ-F1* mutants at 8 h APF. *In vitro* live imaging was performed in one of the pair by confocal microscopy with 50 μM ecdysone in culture medium. (*B*) Time course of caspase activation in wild-type and *βFTZ-F1* mutant salivary glands with or without ecdysone *in vitro*. In each experiment, the average ratio between the anterior, middle, and posterior region was calculated. Average ratio in individual salivary gland was plotted in *B*. To compare wild-type and mutant animals, the emission ratio was normalized by defining the ratio shown in 0 h as 1. Live imaging of at least three salivary glands in each experiment was performed for 17 h or until the cells were completely destroyed. Note that no caspase activation was observed without ecdysone for at least 17 h in wild-type and *βFTZ-F1* mutant salivary glands (*Lower*). The indicated genotypes are: wild-type (*N393/+; UAS-SCAT3/+*) and *βFTZ-F1* mutant (*N393/+; UAS-SCAT3/+; βFTZ-F1^{17}/βFTZ-F1^{19}*).

the emission ratio were detected from 15 h 32 min ± 1 h 30 min APF. Interestingly, in some of the *βFTZ-F1* mutants, caspase activation was significantly delayed and occurred in a random pattern (Fig. 5*A* case 2, arrows; 48%; $n = 21$), in contrast to the anterior-to-posterior wave of activation seen in wild-type controls (Fig. 1). Moreover, the symmetry of caspase activation between the left and right salivary glands was almost completely abolished in these mutants. Some *βFTZ-F1* mutants (19%; $n = 21$) showed an anterior-to-posterior spatial pattern of caspase activation similar to that of wild-type controls; however, these mutants also showed defects in adult head eversion and a marked delay in the initiation of caspase activation (16 h 4 min ± 1 h 12 min).

To examine the caspase activation pattern of the *βFTZ-F1* mutants in detail, we examined caspase activities at the single-cell level, as shown in Fig. 2. In contrast to wild-type controls, the initial caspase activation occurred randomly in *βFTZ-F1* mutants (Fig. 5*BC*). This random activation was confirmed in isolated salivary glands (Fig. 5*BD*). These results strongly suggested that *βFTZ-F1* and the normal ecdysone pulse are involved not only in the temporal regulation but also in the spatial regulation of caspase activation *in vivo*.

Normal Response to Ecdysone of Salivary Glands Isolated from *βFTZ-F1* Mutants *in Vitro*. To determine the association between *βFTZ-F1* and the ecdysone response, we examined the response to ecdysone of salivary glands isolated from *βFTZ-F1* mutants (Fig. 6). Salivary glands from wild-type controls and *βFTZ-F1* mutants were maintained in culture for at least 17 h (Fig. 6*B Lower*, −ecdysone). The salivary glands from *βFTZ-F1* mutants showed the same pattern of caspase activation as wild-type controls in live imaging *in vitro* (Fig. 6*A*), and the time courses of the *in vitro* response to ecdysone were similar in both wild-type controls and *βFTZ-F1* mutants (Fig. 6*B Upper*). These results indicated that the *βFTZ-F1* mutant salivary glands have the ability to respond normally to